Originally published as:

Experimental insights into the scaling and variability of local tsunamis triggered by giant subduction megathrust earthquakes

Matthias Rosenau,[1] Rainer Nerlich,[1,2] Sascha Brune,[3] and Onno Oncken[1]

[1]   Giant subduction megathrust earthquakes of magnitude 9 and larger pose a significant tsunami hazard in coastal regions. In order to test and improve empirical tsunami forecast models and to explore the susceptibility of different subduction settings we here analyze the scaling of subduction earthquake-triggered tsunamis in the near field and their variability related to source heterogeneities. We base our analysis on a sequence of 50 experimentally simulated great to giant ($M_w = 8.3$–9.4) subduction megathrust earthquakes generated using an elastoplastic analog model. Experimentally observed surface deformation is translated to local tsunami runup using linear wave theory. We find that the intrinsic scaling of local tsunami runup is characterized by a linear relationship to peak earthquake slip, an exponential relationship to moment magnitude, and an inverse power law relationship to fore-arc slope. Tsunami variability is controlled by coseismic slip heterogeneity and strain localization within the fore-arc wedge and is characterized by a coefficient of variation $C_v \sim 0.5$. Wave breaking modifies the scaling behavior of tsunamis triggered by the largest ($M_w > 8.5$) events in subduction settings with shallow dipping (<1–2°) fore-arc slopes, limits tsunami runup to <30 m, and reduces its variability to $C_v \sim 0.2$. The resulting effective scaling relationships are validated against historical events and numerical simulations and reproduce empirical scaling relationships. The latter appear as robust and liberal estimates of runup up to magnitude $M_w = 9.5$. A global assessment of tsunami susceptibility suggests that accretionary plate margins are more prone to tsunami hazard than erosive margins.

1.   Introduction

[2]   Among a variety of tsunami sources including earthquakes, landslides, volcanic eruptions, explosions and meteorite impacts, tsunamis triggered by giant ($M_w \sim 9$) subduction megathrust earthquakes represent a subset of relatively rare (1–3 events per century [*McCaffrey*, 2008]) but devastating events which rank high on the hazard scale. To anticipate and mitigate the impact of future events and for early warning attempts, tsunami forecast models have been proven to be a practical tool [e.g., *Geist et al.*, 2007]. Such forecast models are based on empirical scaling relationships between runup (the height above mean sea level of the point of maximum inland penetration of the tsunami) and first-order earthquake source parameters available soon after the seismic event, i.e., the location, magnitude, focal

mechanism, and mean slip [*Abe*, 1981, 1995; *Plafker*, 1997]. While being principally reproduced by numerical models [e.g., *Okal and Synolakis*, 2004; *McCloskey et al.*, 2008], the robustness of such scaling relationships toward the high end of the magnitude scale is, however, not well constrained because of the rareness of giant earthquakes in instrumental and historical catalogs. Moreover, epistemic uncertainties are critical for the application of empirical scaling relationships particularly in the near field. These uncertainties are primarily related to the variability of tsunamis related to unpredictable heterogeneities in second-order source parameters (e.g., details of the slip distribution [*Geist and Dmowska*, 1999; *Geist*, 2002]). Constraints on the latter are thus highly valued but impossible to sample in a statistically relevant, long-term context (over multiple seismic cycles) in nature because of the infrequent occurrence of such extreme events.

[3]   Anticipating the impact of future events includes the analysis of susceptibility of active plate margins to tsunami catastrophes. At a regional scale, tsunami susceptibility of an active plate margin is controlled primarily by the maximum size of possible earthquakes and the long-wavelength bathymetry between the trench and coast that controls tsu-

---

[1]Department of Geodynamics, Helmholtz-Centre Potsdam, GFZ German Research Centre for Geosciences, Potsdam, Germany.
[2]Now at Simula Research Laboratory, Lysaker, Norway.
[3]Department of Physics of the Earth, Helmholtz-Centre Potsdam, GFZ German Research Centre for Geosciences, Potsdam, Germany.

nami shoaling. The maximum size of an earthquake in a subduction zone is controlled by the megathrust geometry and thermal structure [e.g., *McCaffrey*, 2008]. The long-wavelength bathymetry of the subduction zone fore arc is primarily controlled by tectonic mass transfer processes like subduction accretion and erosion [e.g., *Clift and Vannucchi*, 2004].

[4] In order to improve tsunami forecast models we here simulate and analyze the tsunami scaling behavior in the near field of the source (local tsunamis). We do this in a long-term context (i.e., over repeating events) and at the high end of the earthquake magnitude range ($8.2 < M_w < 9.5$). Our objective is to test and modify empirical scaling relationships in a probabilistic manner by additionally incorporating variability and to gain insight into the factors controlling tsunami scaling behavior in different subduction settings (accretive versus erosive). To do so, we first derive the scaling relationships that link earthquake source parameters to tsunami runup without considering nearshore wave breaking. The influence of wave breaking which effectively reduces tsunami runup is considered in a second scaling variant. We distinguish between both variants by referring to them as "intrinsic" and "effective" scaling relationships, respectively. We base our analysis on a sequence of 50 experimentally simulated great ($M_w > 8.2$) megathrust earthquakes from an elastoplastic analog model. Linear wave theory is used to forward model near-field (local) tsunami runup from the simulated tsunamigenic seafloor deformation. We then explore the simulated scaling behavior in comparison with empirical scaling relationships, historical events and numerical simulations. Applying the modified scaling relationships to various subduction zone settings using published data on fore-arc anatomy and maximum earthquake size finally provides constraints on the global pattern of tsunami susceptibility.

[5] We emphasize that this study focuses on tsunamis triggered by giant subduction megathrust earthquakes. It is explicitly not intended to give insight into tsunamis triggered by other sources. Among those sources not considered here are, e.g., slow and shallow "tsunami earthquakes" as well as triggered landslides which are characterized by source characteristics very distinct to those of giant megathrust earthquakes [e.g., *Kanamori*, 1972; *Geist and Bilek*, 2001; *Bilek and Lay*, 2002; *Okal and Synolakis*, 2003, 2004].

2. Simulation and Analysis Techniques

2.1. Experimental Earthquake Simulation

2.1.1. Experimental Setup, Model Scaling and Similarity

[6] The experimental setup used in this study is a modification of conventional quasi-two-dimensional sandbox setups [e.g., *Lohrmann et al.*, 2003] monitored from one side with an industrial strain analysis system (particle image velocimetry, PIV). The experimental method has been described in detail by *Rosenau et al.* [2009]. Here we recall the basics of the approach and report modifications specific to the present study. The experimental device consists of a glass-sided box (1000 mm long × 500 mm high × 100 mm wide) with an inclined basal conveyer plate on top of which a compressive wedge (subduction fore-arc model) is set up

at appropriate scale and compressed against a rigid back wall (Figure 1). Dynamic similarity of the laboratory-scale model with the natural prototype requires the ratios of forces, which are expressed as dimensionless numbers, to be the same as in nature. We use the following set of dimensionless numbers to ensure similarity with respect to strength σ, gravity G, and inertia I:

[7] 1. The ratio τ between gravitation and strength (either elastic, frictional, or viscous) is

$$\tau = \rho\, l\, g/\sigma \qquad (1)$$

where ρ is the rock density, l is a characteristic length, g is the gravitational acceleration, and σ is the elastic, frictional or viscous strength.

[8] 2. The Froude number Fr relates gravitation and inertia and is

$$Fr = v(g\, l)^{-0.5} \qquad (2)$$

where v is a characteristic velocity.

[9] 3. The Cauchy number Ca relates inertia and elasticity and is

$$Ca = \rho\, v^2/k \qquad (3)$$

where k is the bulk modulus.

[10] By keeping these dimensionless numbers the same in an experiment executed in the Earth's gravity field as in nature, the following scaling relationships are derived from equations (1) to (3):

$$\tau^* = \tau \rightarrow \left(\sigma^*/\sigma\right) = \left(\rho^*/\rho\right)\left(l^*/l\right) \qquad (4)$$

$$Fr^* = Fr \rightarrow \left(t^*/t\right) = \left(l^*/l\right)^{0.5} \qquad (5)$$

$$Ca^* = Ca \rightarrow \left(k^*/k\right) = \left(\rho^*/\rho\right)\left(l^*/l\right)^2\left(t/t^*\right)^2 \qquad (6)$$

where asterisk marks the model numbers and values. The ratios between model and natural prototype values are known as the scaling factors [*Hubbert*, 1937].

[11] These scaling relationships dictate the experimental conditions and material properties (Table 1) for a given length scale and density. The model used here is three times less dense and designed at a length scale $(l^*/l) = 3.3 \times 10^{-6}$ such that 1 cm in the model corresponds to 3 km in nature. According to equations (4)–(6) it follows that the model has to be weaker than the natural prototype by a factor $(\sigma^*/\sigma) = 1.1 \times 10^{-6}$ and should deform ~500 times slower during analog earthquakes in order to properly scale the body forces. The corresponding coseismic time scale is $(t^*/t) = 1.8 \times 10^{-3}$ (i.e., 0.1 s in the lab corresponds to about 50 s in nature). Because this time scale would result in unsuitable long recurrence intervals of analog earthquakes in the laboratory and because inertial forces can be neglected during the interevent time we scale the interseismic periods differently with a factor of 1.3×10^{-10} (1 s in the lab scales to ~250 years). Analogue model parameters, experimental conditions and similarity criteria are listed in Table 1. Note
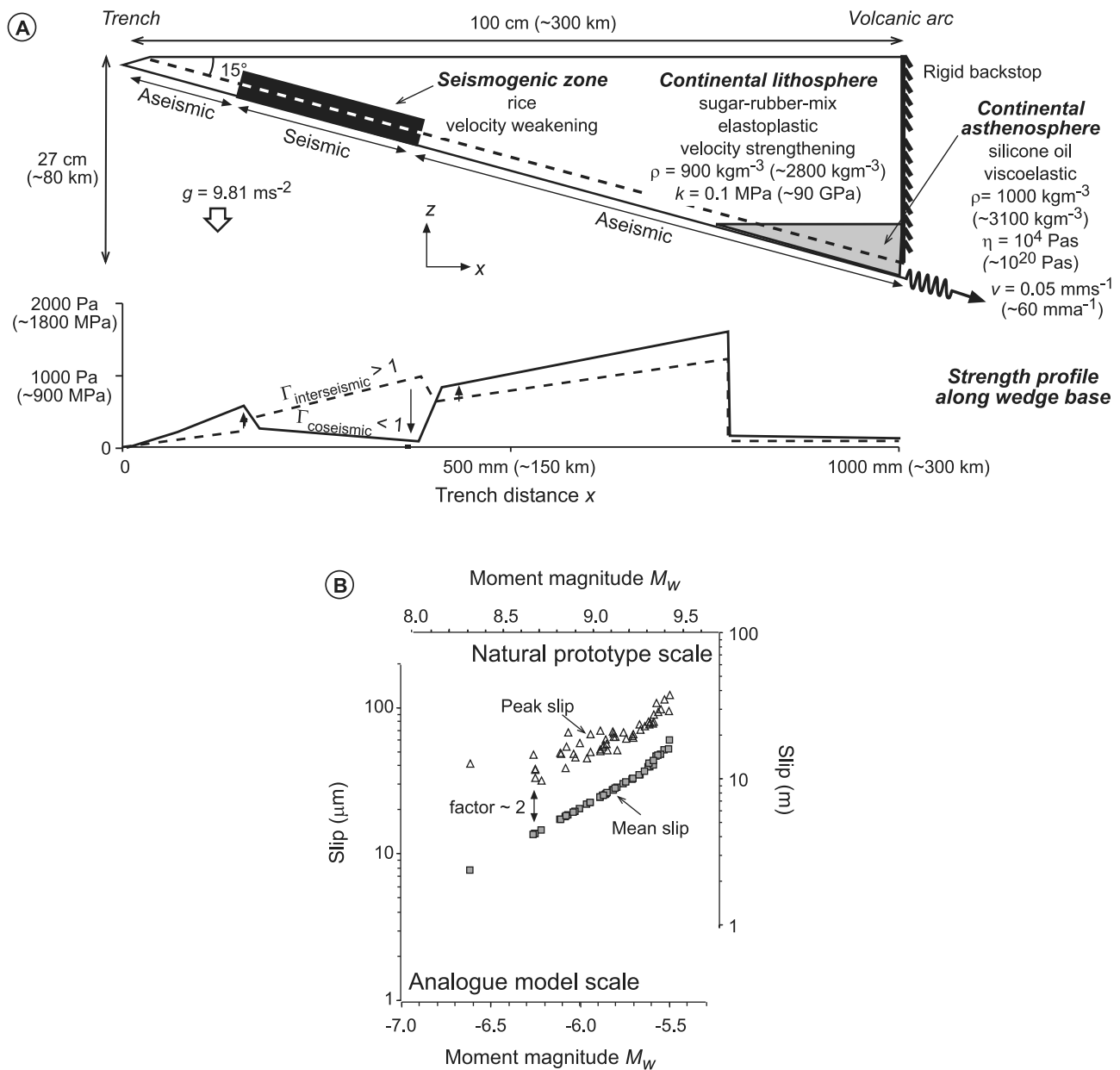
Figure 1. Analogue model setup and scaling. (a) Cross-sectional configuration of the analog model (values in parentheses refer to the parameter value at natural scale). Due to rate-and-state-dependent frictional properties at the wedge base, the strength profile along the megathrust is transient at seismic cycle scale with a relatively strong seismogenic zone (SZ) during the interseismic period (strength contrast between the SZ and surrounding aseismic parts $\Gamma > 1$) and a relatively weak ($\Gamma < 1$) SZ in the coseismic stage. (b) Slip-magnitude relationship of simulated megathrust earthquakes at laboratory (lower left coordinate system) and natural (upper right coordinate system) scale. Note the linear slip-magnitude scaling and the factor of 2 difference between mean and peak slip. See notation for abbreviations used.

that analog models represent strong simplifications of the natural prototype and their application is always limited. With the present model we focus on coseismic subduction fore-arc deformation, i.e., a short-term and large-scale process. This allows for accepting limitations in similarity with the natural prototype regarding small-scale and/or long-term processes. Among those are for example pore fluid diffusion, isostasy as well as erosion and sedimentation.

2.1.2. Analogue Model Configuration, Experimental Conditions, and Material Properties

[12] The generalized subduction zone model presented here is analogous to a 300 km wide fore-arc section from the trench to the volcanic arc. The analog model is made up of a granular wedge of elastic-frictional plastic (elastoplastic) mixtures of EPDM (ethylene propylene diene monomer) rubber pellets with refined sugar and flavored rice representing the brittle fore-arc lithosphere. The wedge overlies silicone

Table 1. Analogue Model Parameters and Similarity[a]

Parameters				Similarity				
Quantity	Symbol	Dimension (M, L, T)	Unit	Quantity	Model	Nature	Dimensionless Number	Scaling Factor
Model Kinematics								
Length	l	L	m	coseismic slip	29 ± 12 μm	8.8 ± 3.6 m	$Fr = v'[gl]^{-0.5}$	3.3×10^{-6}
Velocity (interseismic)	v	L/T	m/s	plate velocity	50 μm/s	60 mm/yr		2.6×10^{4}
Velocity (coseismic)	v'	L/T	m/s	rupture velocity	>3 m/s	>2 km/s	$Ca = \rho v'^2/k$	1.8×10^{-3}
Gravitational acceleration	g	L/T^2	m/s^2		9.81 m/s^2	9.81 m/s^2	g/a'	1
Coseismic slip acceleration	a'	L/T^2	m/s^2		0.6 m/s^2	0.6 m/s^2	g/a'	1
Material Properties								
Friction coefficient	μ			interseismic	0.7	0.7	φ	1
Friction rate parameter	a-b			strengthening/ weakening	±0.015	±0.015	a-b	1
Cohesion	C	M/LT^2	Pa	lithosphere	10 Pa	9 MPa		1.1×10^{-6}
Bulk modulus	k	M/LT^2	Pa	lithosphere	0.1 MPa	90 GPa		1.1×10^{-6}
Viscosity	η	M/LT	Pa s	asthenosphere	10^4 Pa s	7×10^{19} Pa s		1.4×10^{-16}
Density	ρ	M/L^3	kg/m^3	lithosphere/ asthenosphere	900/1000 kg/m^3	2800/3100 kg/m^3		3.3×10^{-1}
Forces								
Gravitation	$G = \rho Vg$	ML/T^2	N					1.2×10^{-17}
Inertia	$I = \rho Va$	ML/T^2	N					1.2×10^{-17}
Energy								
Seismic moment	$M_0 = kDA$	ML^2/T^2	N m	seismic moment	3 ± 2 N m	$7 \times 10^{22} \pm 5 \times 10^{22}$ N m		4×10^{-23}

[a]See notation section for parameters used.

oil representing the viscoelastic asthenosphere (Figure 1 and Table 1). We generalized the natural subduction geometry by considering a planar, 15° dipping megathrust between an upper plate made up of ~60 km thick lithosphere and ~20 km thick asthenosphere and an oceanic plate. The latter is represented by a conveyer plate pulled constantly via a spring-loaded thrust pad (k = 8 MPa) at 50 μm/s simulating plate convergence at a long-term rate of about 60 mm/yr in nature. The experimental run took place under normal gravity conditions and in a dry room climate (22–23°C, 30–40% humidity).

[13] Material properties have been measured using a ring-shear tester (static and dynamic friction coefficients, cohesion, and density), a uniaxial compression tester (bulk modulus) and a cone-plate rheometer (viscosity) as described by *Rosenau et al.* [2009] and reviewed here for completeness. Accordingly, the model densities are 900 kg/m^3 and 1000 kg/m^3 for the wedge lithosphere and asthenosphere, respectively, scaling to ~2800–3000 kg/m^3 in nature. Elasticity of the model lithosphere is characterized by bulk modulus k of about 0.1 MPa (~90 GPa in nature). Viscosity of the model asthenosphere is about 10^4 Pa s (~10^{19} Pa s in nature) and characterized by weak shear rate thinning (allowing strain localization) and very short (<10 ms) Maxwell relaxation time (suppressing postseismic relaxation effects) [*Rosenau et al.*, 2009].

[14] The model megathrust is defined by a few millimeters wide shear zone which forms at the base of the wedge ("subduction channel" [*Shreve and Cloos*, 1986]). It is characterized by a transient strength profile controlled by rate- and state-dependent frictional behavior similar to nature [*Scholz*, 1998; *Oleskevich et al.*, 1999]. In particular, it includes a shallow (15–30 km depth) seismogenic zone

(SZ) of stick-slip deformation. Stick slip in the model mimics alternating interseismic locking (or minor creep) and seismic slip and is controlled by the velocity weakening behavior of frictional slip in rice. The latter is characterized by a friction coefficient of $\mu \sim 0.8$ in the interevent ("stick") period which drops toward zero during episodic slip events. The friction rate parameter a-b within the seismogenic zone is ~−0.015. The seismogenic zone is limited updip and downdip by "aseismic" zones of stable sliding (creep) controlled by the velocity strengthening behavior (a-b ~+0.015) of frictional slip in sugar ($\mu \sim 0.7$). A velocity strengthening sugar-rubber mixture makes up the fore-arc lithosphere. Cohesion of the granular materials used is low (in the order of 10 Pa). The resulting time variable relative strength Γ of the seismogenic zone with respect to the aseismic areas along the base and of the wedge interior controls the accumulation and release of elastic strain (stress) as well as the plastic deformation of the wedge. Γ is >1 during the interevent (stick) period corresponding to a relatively strong (locked) seismogenic zone during the interseismic period allowing for convergence-induced stresses to be transmitted across a frictionally coupled plate interface and to deform the wedge both elastically and plastically. Γ is <1 during episodic slip events representing a relatively weak seismogenic zone during the coseismic stage of the subduction earthquake cycle when unlocking of the plate interface allows convergence-induced stresses to be released.

2.1.3. Experimental Monitoring and Strain Analysis

[15] For strain analysis of the evolving model wedges we use an optical image acquisition and correlation system (particle image velocimetry, PIV StrainMaster by LaVision, Germany; see *Adam et al.* [2005] and *Rosenau et al.* [2009] for applications in analog tectonic and earthquake simula-

tion). During an experiment, the locations of particles on one side (i.e., within the x-z plane of the model, Figure 1) are recorded by sequential 11 Mpx digital images of a 14-bit monochrome charge-coupled device (CCD) camera acquired at a frequency of 10 Hz. The x-z displacement vector field between successive images is then determined by cross correlation of textural differences (i.e., gray values) formed by groups of particles using a fast Fourier transform algorithm. In the present setup the spatial resolution of the final displacement vector grid is ~3 mm or about 1 km in nature. For each grid cell, an average x-z displacement vector is determined at micrometer precision (approximately decimeter scale in nature). This allows for observing episodic slip events corresponding to earthquakes of moment magnitude $M_w >$ 7–8. Analogue earthquakes are characterized by episodic, usually more than one order-of-magnitude increased strain rates and a change in polarity of the wedge deformation (mainly extension) compared to the wedge deformation during loading (mainly shortening). They typically occur within a 0.1 s time interval, i.e., are captured by a single PIV image.

2.1.4. Analogue Earthquake Moment Scaling

[16] In order to scale our two-dimensional (x-z plane) experimental observations of analog earthquake source parameters (mean and maximum or peak slip, rupture width) to the three-dimensional quantities of seismic moment M_0 and moment magnitude M_w, we infer a lateral (parallel to the y axis of the model or trench-parallel-directed in nature) rupture length following the procedure described by *Rosenau et al.* [2009]. This involves the assumption of laterally uniform moment distribution (i.e., we neglect possible lateral segmentation of the rupture) and application of an empirical scaling law of the form:

$$L = 6.5 \times 10^9 \times \text{ mean slip}^{1.2}/W \qquad (7)$$

where L and W are the rupture length and width, respectively. Equation (7) has been derived originally by *Rosenau et al.* [2009] by regression analysis of empirical rupture area and average slip data of $M_w > 7$ subduction megathrust earthquakes presented by *Cloos* [1992]. We limit hypothetical rupture lengths to 1300 km which corresponds to the average maximum length of possible earthquakes in subduction zones of the earth delimited by the average maximum trench length [*Clift and Vannucchi*, 2004; *McCaffrey*, 2008]. Eventually, seismic moment M_0 has been derived as the product of mean slip, rupture area and rigidity. The error in M_0 of simulated events that arises from the monitoring resolution limits and uncertainties in the mechanical properties of the analog model scales to about 5×10^{19} N m which is <2% of the seismic moment of the earthquakes studied here ($M_w > 8.2$).

2.2. Tsunami Model

[17] We use an analytical tsunami model to explore the first-order scaling and variability of tsunami waves in the near field triggered by great megathrust earthquakes. To characterize local tsunamis, we derive tsunami runup h directly from the surface deformation shown by the analog model through linear wave theory following *Synolakis* [1987, 1991]. Because coseismic seafloor deformation during great megathrust earthquakes is dominated by uplift [e.g., *Plafker*,

1972; *Meltzner et al.*, 2006], we base our tsunami model on a cnoidal solitary wave form (sech^2 model according to *Synolakis* [1987, 1991]), i.e., as a crest only. We do not model a leading trough or depression wave (N wave [*Tadepalli and Synolakis*, 1994, 1996]) because peak seismic slip typically occurs close to the coast in the model as in nature resulting in coseismic subsidence either onshore or limited to shallow water near the coast [e.g., *Plafker*, 1972]. Coseismic subsidence is therefore not considered to be tsunamigenic here. For the coseismic seafloor deformations simulated here this assumption is supported by comparison with an alternative, numerical tsunami model simulating the full wave form as described in the auxiliary material.[1] N wave models result in about 1/3 higher runup compared to solitary wave models [*Tadepalli and Synolakis*, 1994, 1996] and have been shown to be more appropriate to model local tsunamis from "tsunami earthquakes" [*Kanamori*, 1972; *Geist and Bilek*, 2001; *Bilek and Lay*, 2002] where seismic slip closer to the trench causes deep water seafloor subsidence.

[18] The initial tsunami wave height H at the source is assumed to be the same as the static coseismic seafloor uplift in the source region [*Tanioka and Satake*, 1996]. This static approach is justified because the phase velocity of tsunami waves is much less (about an order of magnitude) than earthquake rupture velocity [*Tanioka and Satake*, 1996]. Seafloor uplift includes components from both the vertical ($\mathrm{d}u_z$) and horizontal ($\mathrm{d}u_x$) coseismic surface displacements:

$$H = \mathrm{d}u_z + \mathrm{d}u_x \tan \phi \qquad (8)$$

where ϕ is the average fore-arc slope [*Tanioka and Satake*, 1996]. Because the trench-normal coastal distance of tsunamigenic seafloor uplift is generally <150 km we omit simulating the wave propagation stage and calculate directly the amplification of a solitary wave due to shallowing water along a constant gradient. According to linear wave theory [*Synolakis*, 1987, 1991] the tsunami height increases as the wave climbs up the fore-arc wedge and coastal runup h follows as:

$$h = 2.831(\cot \phi)^{1/2} H^{5/4} d^{-1/4}, \qquad (9)$$

where the water depth d at the source is calculated from the distance between the tsunamigenic seafloor uplift and the coast as a function of fore-arc wedge slope ϕ. Sensitivity analysis indicates that the error in the runup estimates that arises from laboratory measurement uncertainties in H and d from the analog model is <10%.

[19] Because waves will break when a certain height to water depth ratio is exceeded, maximum tsunami height is naturally limited. *Synolakis* [1991] noted that the runup law (equation (9)) strictly applies only to waves which satisfy

$$h < h_{\max} = 0.818(\cot \phi)^{-10/9} \qquad (10)$$

In the present study we use this breaking criterion as a limit criterion. Accordingly, we compare the runup h predicted by the runup law (equation (9)) with the limit height $h_{\max}$ given

---

[1]Auxiliary materials are available in the HTML. doi:10.1029/2009JB007100.

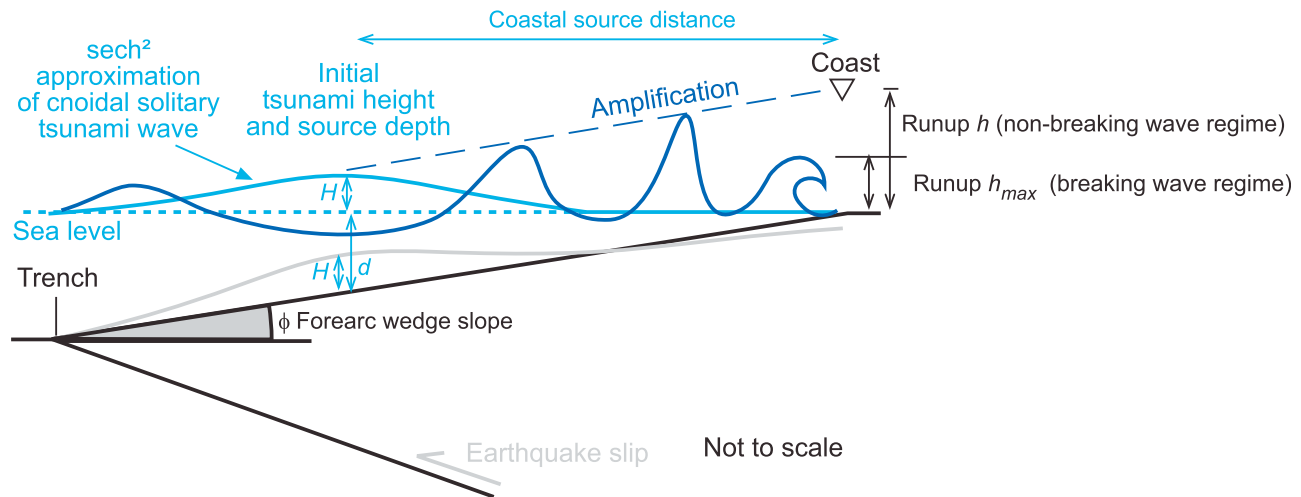**Figure 2.** Parameters of the tsunami model used here. See text for explanation and notation for abbreviations used.

by equation (10). For $h < h_{max}$ we use the original runup h for prediction, for $h > h_{max}$ we use the limit height h_{max} for prediction (Figure 2). Importantly, the latter may overestimate actual runup as broken waves (tsunami bores) tend to show smaller runup than predicted by solitary wave runup [*Yeh*, 1991]. In order to examine earthquake-triggered tsunami scaling behavior, we therefore compare the predictions of these two tsunami models: Application of equation (9)) results in the model of the "intrinsic" scaling behavior of tsunamis, whereas the combination of equations (9) and (10) results in a modified model describing the "effective" scaling behavior (which can be related to natural runup observations). We note that the first variant is instructive in terms of illustrating the principles of earthquake-triggered tsunamis, but the latter is that important for tsunami forecast. We cross-validated the results of the analytical tsunami model used here with a simulation described in the auxiliary material.

[20] It is noteworthy that the model we use remains simplistic as we neglect a variety of complexities well known to occur in nature. For instance, we do not take into account the effects bathymetric slope changes across the fore arc and any high-order bathymetric complexities such as canyons, cliffs or estuaries. The latter are important for susceptibility analysis at a local scale but not considered in the present large-scale analysis. In order to isolate the effects of source heterogeneity we use the simplest parameterization of bathymetry; that is, we assume a constant slope from the offshore tsunami source to the coast. Moreover, we consider only the tsunami phase directly from the source; that is, we neglect reflected and trapped edge waves that may occasionally have larger amplitudes than the first arrival [e.g., *González et al.*, 1995]. For those waves identified as breaking waves we furthermore omit predicting the exact runup of tsunami bores which is generally lower than the unbroken wave [*Yeh*, 1991] and instead use the maximum wave height as limited by equation (10) as a maximum runup estimate (liberal estimate).

2.3. Scaling and Variability Analysis

[21] Based on the sequence of simulated tsunamis we explore the tsunami scaling behavior and its associated variability by means of regression analysis using the least squares method. We apply different regression models (linear, exponential, logarithmic, power law) and use the coefficient of determination R^2 as goodness of fit parameter in model selection. In particular we regressed tsunami runup against peak slip ($h(\delta u)$ scaling) as well as against moment magnitude ($h(M_w)$ scaling). The regression model which maximizes R^2 is inferred to provide the best mathematical description of the intrinsic scaling behavior. Tsunami variability is finally characterized by the coefficient of variation C_v, which is the standard deviation divided by the mean value, for any given earthquake source parameter.

3. Experimental Observations and Analysis Results

3.1. Seismotectonic Performance of the Model Wedge

3.1.1. Long-Term Deformation

[22] After an initial phase of elastic loading of the system, material compaction, and strain localization, the model wedge mimics about 175 ka of seismotectonic evolution of a subduction zone fore arc. The result is a model fore-arc wedge with a morphostructural inventory similar to natural subduction zones and intrinsically related to the distribution of stable and unstable (stick) slip along the basal megathrust (Figure 3). In particular, convergence-induced, permanent shortening peaks near the wedge tip and decreases systematically toward the rear of the wedge consistent with first-order strain patterns of natural prototypes [e.g., *von Huene and Klaeschen*, 1999; *Nicol and Beavan*, 2003]. Although the finite strain pattern of the model wedge does not resolve the structural details of its natural prototype, e.g., single faults within the accretionary wedge, the principal morphostructural elements can be interpreted.

[23] At the wedge base, an up to about 10 mm wide shear zone represents a few kilometer wide subduction channel [*Shreve and Cloos*, 1986] in nature which includes a seismogenic zone of unstable stick-slip deformation (earthquakes). Permanent strain localizes within the wedge updip and downdip of the seismogenic zone in the form of, respectively, seaward and landward verging thrusts and back
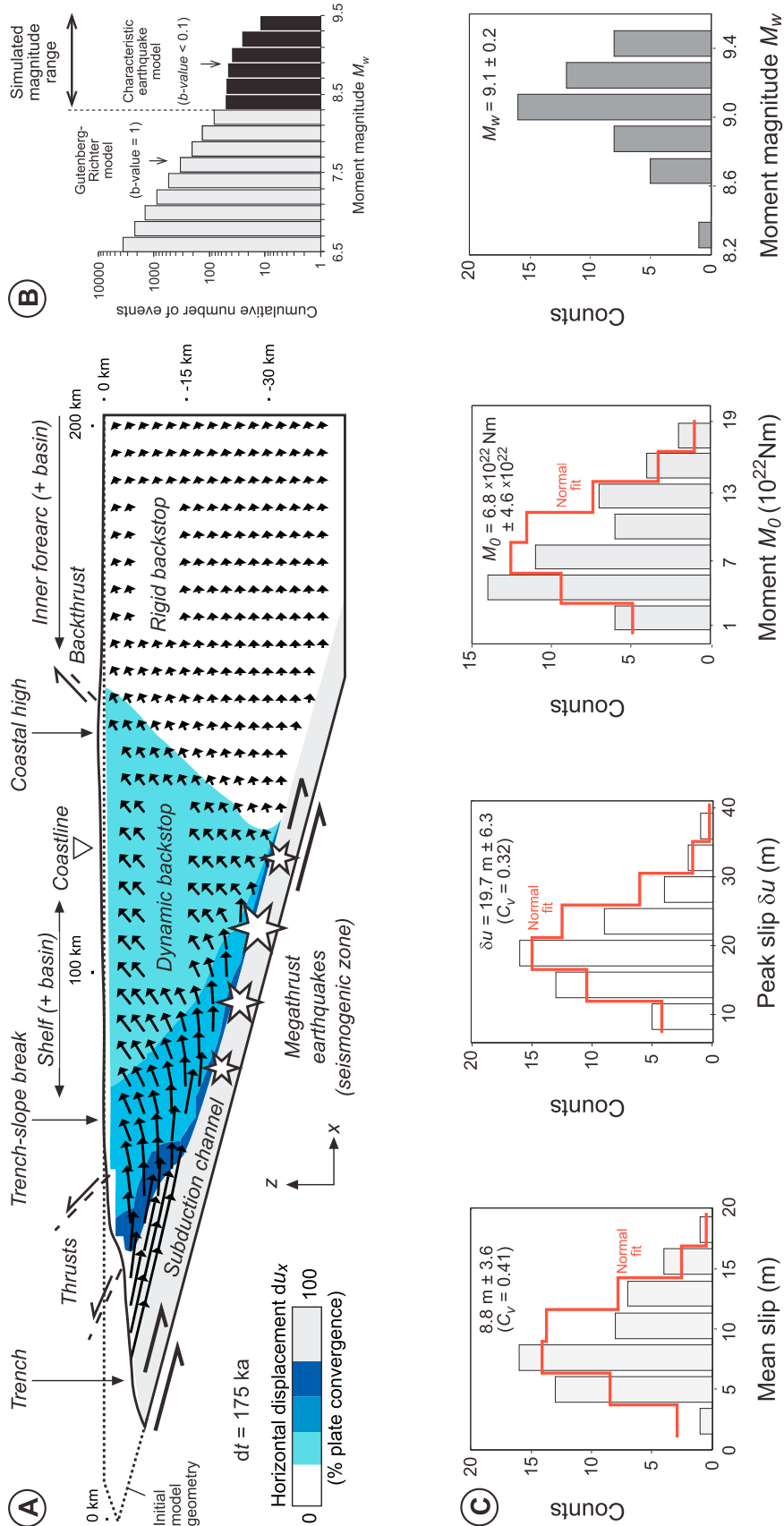
Figure 3. Seismotectonic performance of the analog model: (a) Finite displacement field and long-term seismotectonic deformation pattern, (b) cumulative frequency-magnitude distribution of simulated earthquakes (black bars) plotted together with a hypothetical Gutenberg-Richter relationship (gray bars, slope equal to b value of 1) at smaller magnitudes, and (c) size distributions of simulated earthquakes by means of mean and peak slip, seismic moment, and moment magnitude. Note the low b value (<0.1), low coefficients of variation (C_v < 0.5), and the unimodal character of the size distributions (normal distribution fit shown for comparison) indicating a characteristic earthquake model behavior. All parameter values are given at natural scale.
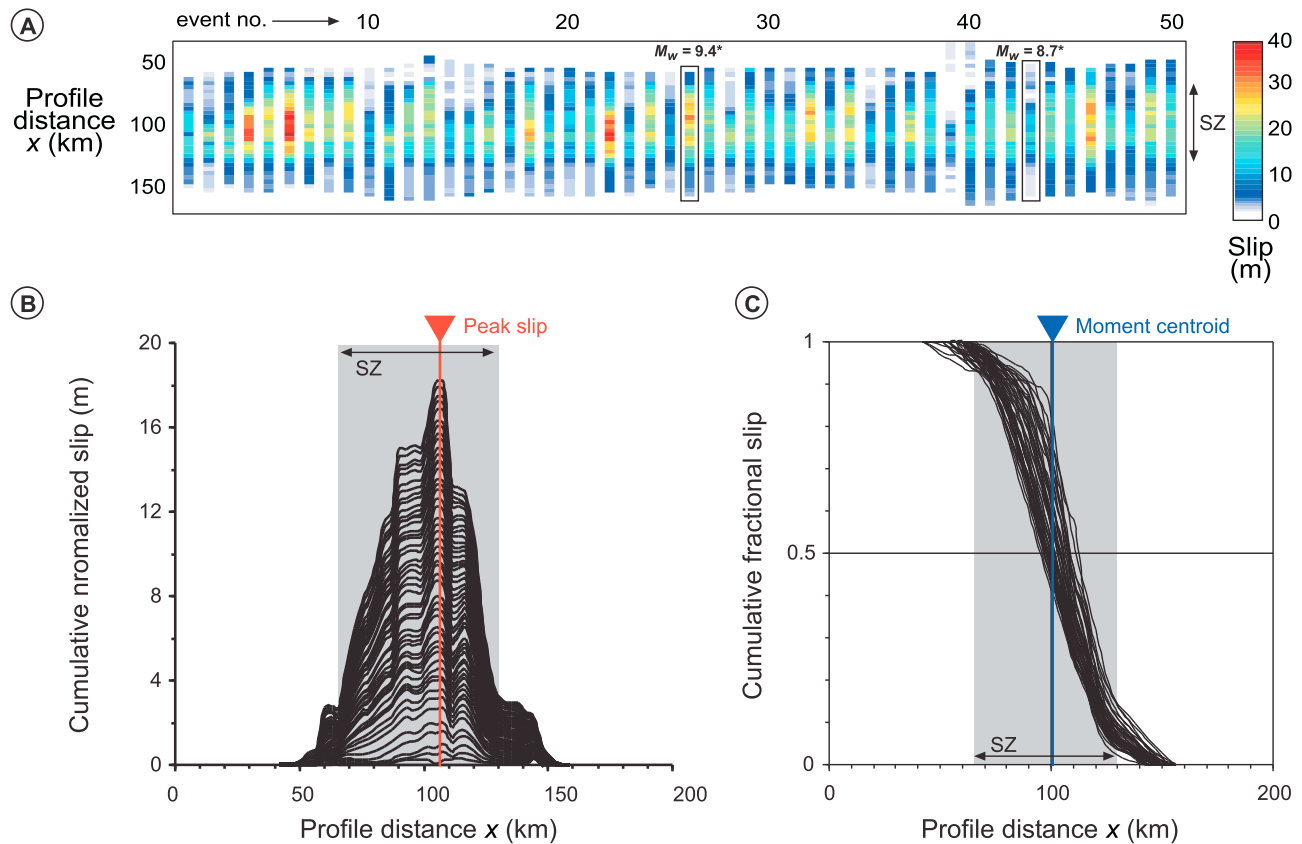
Figure 4. Source parameters of the sequence of 50 earthquakes used in this study: (a) slip distributions, (b) normalized, cumulative slip distribution, and (c) cumulative fractional slip distribution (all parameter values are given at natural scale; asterisk denotes earthquake examples shown in Figure 5). Note that major earthquake slip is limited to the seismogenic zone (SZ) and that a skewed, bell-shaped slip distribution emerges over multiple events consistent with theoretical crack-like slip distribution.

thrusts. Seaward verging thrusts accommodate a dominant part of plate convergence and represent accretionary wedge thrusts and splay faults in nature [e.g., *Park et al.*, 2002]. The latter controls the location of the trench slope break. Back thrusting controls uplift of a coastal high or, where the inner fore arc is submerged, an island chain [e.g., *Chauhan et al.*, 2009; *Singh et al.*, 2010] against an undeformed ("rigid") backstop [*Byrne et al.*, 1988]. The latter forms the continental basement of an inner fore-arc basin [e.g., *Chauhan et al.*, 2009; *Klingelhoefer et al.*, 2010]. Seaward verging thrusts and landward verging back thrusts enclose a bivergent wedge-shaped, internally less deformed domain which corresponds to a "dynamic" backstop [e.g., *Kopp and Kukowski*, 2003] and represents the shelf and coastal region in nature. Large parts of this domain overlie the seismogenic zone in nature and often have basins associated with them [e.g., *Wells et al.*, 2003; *Wang and Hu*, 2006]. The model coastline roughly coincides with the downdip limit of the seismogenic zone similar to nature [*Ruff and Tichelaar*, 1996].

3.1.2. Earthquakes and Coseismic Fore-Arc Deformation

[24] During the experimental run the model wedge has generated detectable episodic slip events which are interpreted as megathrust earthquakes and which scale to events larger than magnitude $M_w \sim 8$. In order to focus our analysis on typical great to giant tsunamigenic megathrust earth-

quakes, we separated 50 events for further analysis which satisfy the following criteria: (1) they nucleate within the seismogenic zone, i.e., at a depth >15 km in nature, (2) they are of moment magnitude larger than $M_w = 8.2$ if scaled to nature using the fault length calculated from equation (7), (3) they saturate the seismogenic width of the subduction interface in less than 50 s in nature (i.e., one single 0.1 s long incremental PIV image in the experiment) or with a mean rupture velocity >2 km/s if scaled to nature, and (4) the deformation field captured by PIV reflects the static coseismic deformation. We choose criteria 1 to 3 in order to eliminate very shallow and slow slip events which overlap in their source characteristic with events generally classified as tsunami earthquakes in the strict sense [*Kanamori*, 1972; *Geist and Bilek*, 2001; *Bilek and Lay*, 2002]. Criterion 4 assures that our results are not biased by dynamic deformation patterns.

[25] Scaled moment magnitudes of the thus separated simulated megathrust earthquakes range from $M_w = 8.3–9.4$ with a mean moment magnitude of 9.1 ± 0.2 (Figures 1b and 3b) when equation (7) is applied. Note that a maximum moment magnitude of $M_w = 9.4$ is consistent with the mean maximum subduction zone earthquake predicted by *McCaffrey* [2008]. Mean slip during simulated earthquakes ranges from 2.3 m to 18 m around an average of 8.8 m with a coefficient of variation (the standard deviation divided by
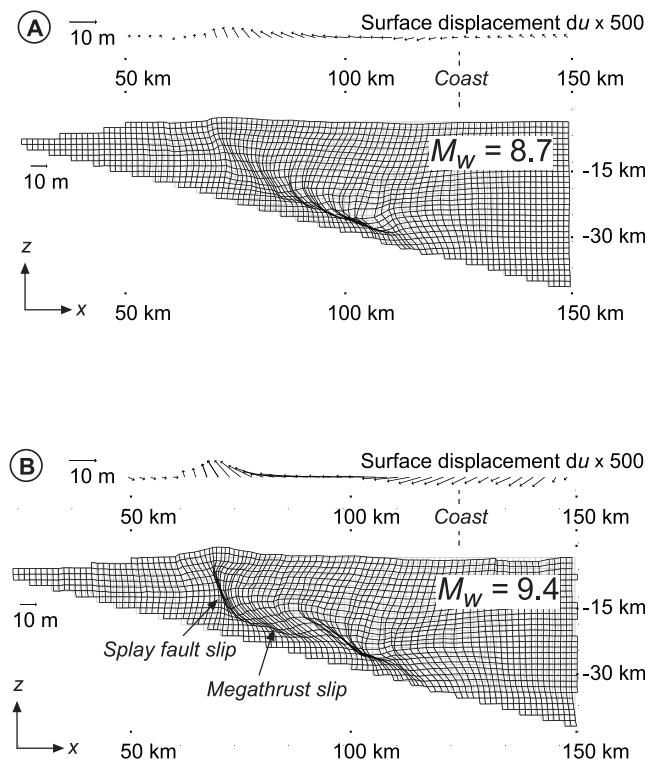
Figure 5. Examples of static coseismic fore-arc deformation patterns during simulated great megathrust earthquakes: Surface deformation and deformed grids of (a) magnitude $M_w = 8.7$ and (b) magnitude $M_w = 9.4$ megathrust earthquakes (all parameter values are given at natural scale). Note exaggerated scale of vectors and grid deformation.

the mean) $C_v \sim 0.4$ (Figure 3c). The peak slip is a factor of ~2–2.5 times the mean slip (20 m ± 6 m, $C_v \sim 0.3$, Figures 1b and 3c). The size statistics of simulated earthquakes are characterized by unimodal distributions in terms of slip, seismic moment and moment magnitude (Figure 3c) resulting in a flat slope of the cumulative frequency-magnitude distribution (b value < 0.1) compared to a typical Gutenberg-Richter distribution (b value = 1, Figure 3b). Unimodal size distributions, low coefficients of variation as well as a low b value indicate that simulated great to giant megathrust earthquakes follow a characteristic earthquake model where the largest events occur more frequently than predicted by the Gutenberg-Richter relationship for smaller events. Characteristic type earthquake recurrence behavior has also been invoked for the greatest subduction zone earthquakes in nature and seems to be related to the simple fault geometry and generally low amounts of permanent fore-arc deformation above the seismogenic zone [e.g., *Rosenau and Oncken*, 2009, and references therein].

[26] The 50 events used for the present analysis show first-order similarities and second-order heterogeneities in slip distribution and coseismic fore-arc deformation which will control the intrinsic scaling and variability of the tsunamis modeled below, respectively, and are therefore described here in detail. To first order, the simulated megathrust earthquakes share a bell-shaped slip distribution and bipolar surface deformation patterns (Figures 4–6). Rupture propagation into the velocity strengthening part of

the megathrust is effectively limited both updip and downdip of the seismogenic zone to a few tens of kilometer (Figure 4a and 4b). The bell-shaped slip distribution is slightly skewed seaward with the centroid located about 10 km seaward of the peak slip (Figures 4b and 4c). Such a distribution is consistent with crack theory [e.g., *Freund and Barnett*, 1976; *Wang and He*, 2008] and natural observations [e.g., *Hoechner et al.*, 2008; *Moreno et al.*, 2009]. Similar shapes are also frequently used as dislocation input for numerical tsunami simulations [e.g., *Sobolev et al.*, 2007] and appear a valid (physically reasonable) parameterization of (typical) seismic slip in worst case scenarios. The simulated coseismic wedge response to earthquake slip along the megathrust is to first-order similar for all events and characterized by seaward motion of the fore arc, subsidence in the coastal region and uplift of the shelf and slope region (Figures 5 and 6). Peak surface motions are in the order of few meters and about one fifth of peak earthquake slip. The pivot line, separating zones of uplift and subsidence, is located about 20 km offshore. This characteristic pattern is consistent with elastic dislocation theory [*Okada*, 1992] and natural observations [e.g., *Plafker*, 1972; *Meltzner et al.*, 2006]. Noticeably, the cnoidal shape of the simulated seafloor uplift and the limitation of subsidence to shallow water or onshore regions (Figure 6b) justify the use of a solitary wave model for tsunami simulation because no significant leading depression wave is triggered by such a deformation pattern.

[27] Apart from first-order similarities of the events, important second-order heterogeneities exist in both simulated earthquake slip distributions and coseismic wedge deformation which presumably exist in nature as well. Such second-order heterogeneities have no significant effect on tsunami scaling but control the variability of the simulated tsunamis. Slip heterogeneity in the model arises primarily from slip deficits accumulated over the prerupture slip history. Heterogeneity in coseismic wedge deformation is controlled primarily by slip partitioning and strain localization. Figure 5 shows two examples of static elastoplastic wedge deformation patterns representative of simulated magnitude 8 and 9 events. During the simulated events slip might be partitioned into slip dislocations parallel to the wedge base (megathrust slip). Due to the velocity strengthening frictional behavior of the wedge material we observe no surface ruptures in the model. However, during giant events minor slip and strain localization might also occur along dislocations oblique to the wedge base affecting tsunami variability.

3.2. Tsunami Scaling and Variability

[28] Surface deformation observed in the analog model has been used as input into equation (9) to simulate a sequence of tsunami runup for the earthquake moment magnitude range $8.2 < M_w < 9.5$. Based on this sequence we first explore the intrinsic tsunami scaling behavior and its associated variability. Eventually, we apply the limit criterion (equation (10)) in order to mimic the effect of wave breaking for the scaling behavior of the sequence.

3.2.1. Intrinsic Scaling and Variability

[29] For a given fore-arc slope angle ϕ, the predicted tsunamis show a linear relationship between runup h and coseismic peak slip δu (Figure 7a) and a nonlinear rela-
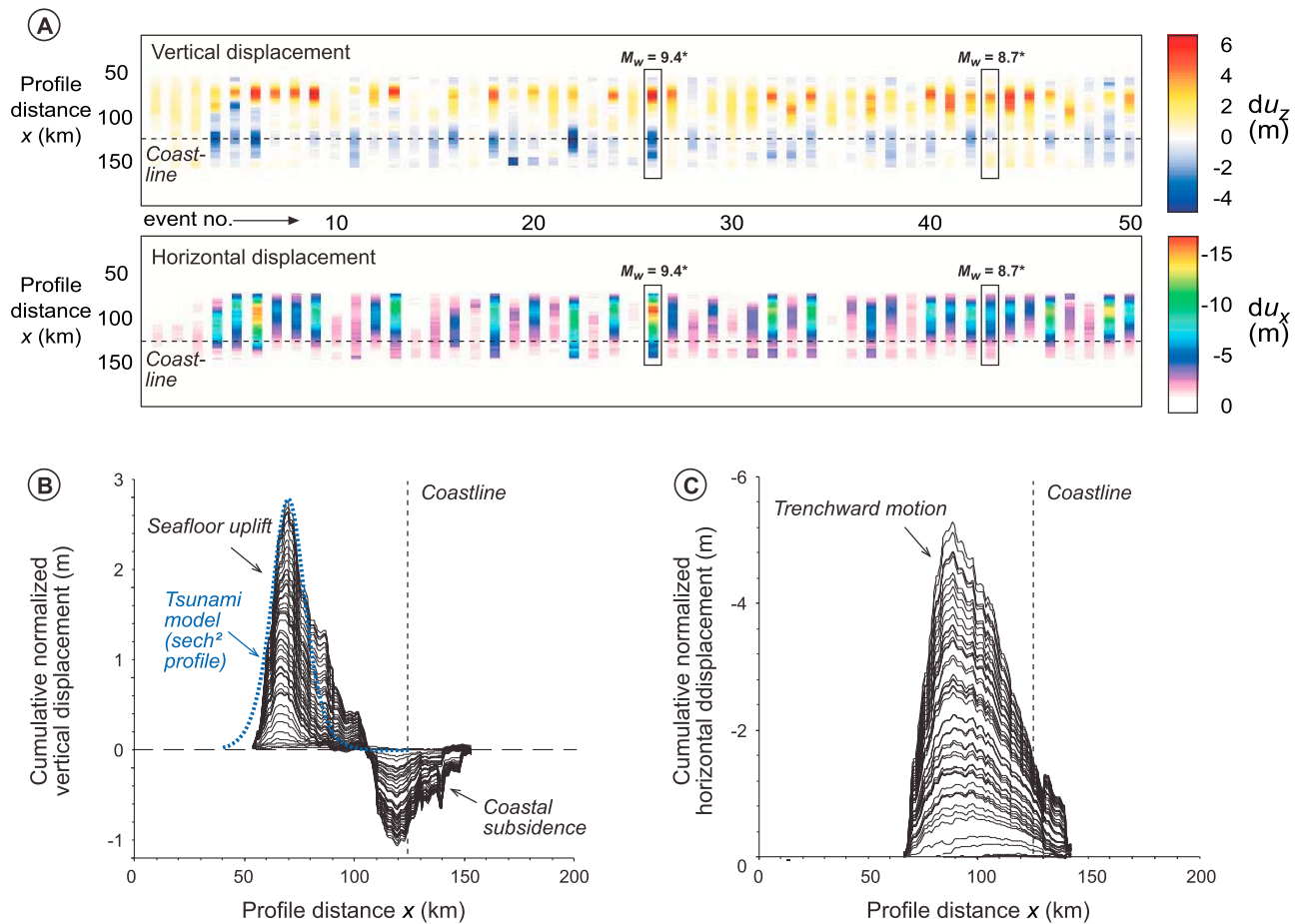
Figure 6. Surface deformations associated with the sequence of 50 earthquakes used in this study as input for the tsunami model: (a) Vertical (du_z) and horizontal (du_x) displacement, (b) normalized, cumulative vertical deformation (the shape of a cnodial solitary wave (sech^2 model) assumed in the tsunami simulation is shown for comparison in blue), and (c) normalized, cumulative horizontal displacement (all parameter values are given at natural scale, asterisk denotes earthquake examples shown in Figure 5).

tionship between h and earthquake magnitude M_w in the nonbreaking wave regime (Figure 7b). The best fit to the $h(\delta u)$ relationship is a linear function ($0.3 < R^2 < 0.4$) with positive abscissa. Linear $h(\delta u)$ scaling is consistent with the principal linear elastic deformation behavior of the model (i.e., surface deformation proportional to basal slip dislocation) and weak nonlinearity (power law exponent 1.25) of equation (9) with respect to the initial wave height H, which is controlled by coseismic seafloor uplift. For a given fore-arc slope, the variability of water depth at the tsunami source, d, which is controlled by the location of coseismic fore-arc uplift is rather small ($C_v \sim 0.2$). This suggests that its role in tsunami scaling behavior is minor. The best fit to the $h(M_w)$ relationship is an exponential function ($0.4 < R^2 < 0.5$). Exponential $h(M_w)$ scaling is related to linear elastic behavior of the model in combination to a weak nonlinearity (power law exponent 1.25) of equation (7) with respect to the peak slip δu, the most variable parameter in our simulation, and the logarithmic moment magnitude scale. Both relationships show a significant scatter which is interpreted to represent the intrinsic variability resulting from a combined effect of earthquake source heterogeneity and coseismic

deformation variability over multiple events. We cross-validated these trends based on a sequence of tsunamis simulated using an alternative model which combines surface deformation of an elastic dislocation model and numerical tsunami simulation as described in the auxiliary material.

[30] In nature a variety of fore-arc wedge geometries exists which is controlled primarily by long-term mass transfer processes like subduction erosion and accretion [e.g., *Clift and Vannucchi*, 2004]. Fore-arc slope varies systematically in these settings as a function of plate convergence and trench sedimentation [*Clift and Vannucchi*, 2004]. At the same time fore-arc slope controls tsunami wave amplification [*Synolakis*, 1987, 1991] and thus a link between tectonic setting and tsunami hazard exists. To explore earthquake-tsunami scaling and variability as well as susceptibility in a wide range of settings, we thus focus on the sensitivity of the earthquake-tsunami scaling relationships to fore-arc slope. We recalculate runup for fore-arc slopes ranging over 2 orders of magnitude ($\phi = 0.1$ to $10°$) covering typical fore-arc wedge geometries (Figures 8 and 9 and Animations S1 and S2 in the auxiliary material).
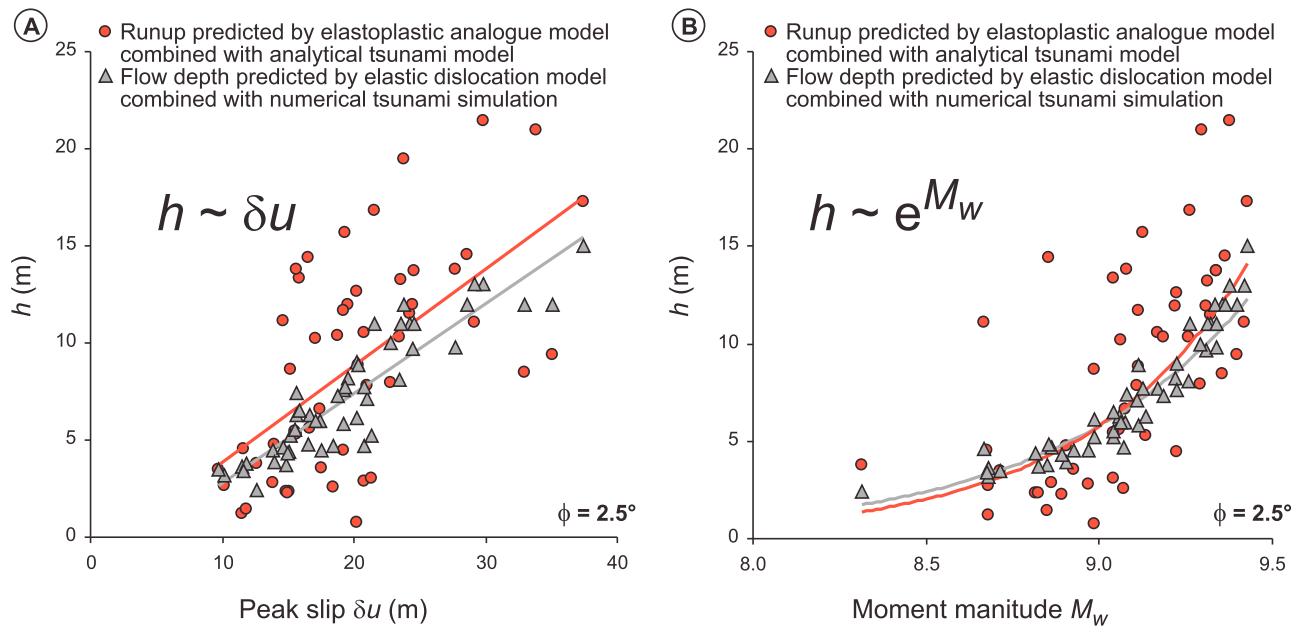
Figure 7. Example of the results of the analytical tsunami model in comparison with predictions of an alternative, numerical tsunami simulation described in the auxiliary material for a 2.5° dipping fore-arc slope: h versus (a) peak earthquake slip δu and (b) moment magnitude M_w (all parameter values are given at natural scale). Best fit regression models indicated (red line indicates original model; gray line indicates alternative model). Both models show similar trends, but the variability is reduced in the numerical simulation which uses an elastic dislocation model as input (neglecting the effect of coseismic deformation variability) in contrast to the analytical tsunami model which uses experimental surface deformation observations (including the effect of coseismic deformation variability). Note that h predicted by the numerical model is flow depth (maximum water height above mean sea level near the beach or above land) not runup (height above mean sea level of the point of maximum inland penetration of the tsunami). Flow depth is calculated here at the 1 m isobath.

[31] Accordingly, the scaling of tsunami runup (in the nonbreaking wave regime) is intrinsically related to peak earthquake slip δu and magnitude M_w via

$$h \sim \alpha \delta u \qquad (11)$$

and

$$h \sim e^{\beta M_w} \qquad (12)$$

for a given slope ϕ with α and β being nonlinear functions of slope. Vice versa, for a given peak slip or magnitude, runup is related to slope via

$$h \sim \phi^{-\gamma} \qquad (13)$$

with γ being nonlinear functions of peak slip or magnitude. The linear runup-slip scaling points to a rather simple relationship between earthquake source and tsunami size. The exponential relationship between runup and moment magnitude is largely controlled by the logarithmic magnitude scale. The inverse power law dependence of tsunami wave runup from slope is a direct consequence of the amplification law (equation (9)). For a given earthquake peak slip or moment magnitude, tsunami runup variability is characterized by a coefficient of variation of $C_v \sim 0.5$ and is a function of slope (Figures 8a and 8b). Variability is minimized for slopes of 2–3° and increases both toward shallower and steeper slopes.

3.2.2. Effective Scaling and Variability

[32] The analysis of intrinsic scaling illustrates the principles of tsunami scaling. However, its applicability to nature is limited because equations (11)–(13) predict unrealistically high tsunami runup (>30 m) along shallow slope margins and for large earthquake magnitudes (Figures 8a, 8b, 9a, and 9b) where waves might break instead. In this section, wave breaking is therefore included in the model in the form of a limit criterion (equation (10)). The thus modified, effective scaling relationships (Figures 8c, 8d, 9c, and 9d) yield tsunami runup more similar to natural observations (<30 m, e.g., NOAA National Geophysical Data Center, NGDC tsunami runup database) and are discussed here in comparison with empirical scaling relationships.

[33] The intrinsic linear $h(\delta u)$ scaling (equation (11)) is qualitatively similar to the widely accepted but informal "Plafker's rule of thumb" [*Okal and Synolakis*, 2004]. Based on empirical analysis, the latter states that local tsunami runup h is in the order of maximum coseismic slip of a simple dislocation source and never exceeds twice the dislocation slip [*Plafker*, 1997]. Applied to more complex source kinematics (such as those simulated here characterized by a ratio of peak to mean slip of about two), the rule suggests that tsunami runup h scales to maximum coseismic slip, δu, by a factor of 0.5–1. Equation (11) fits well this rule
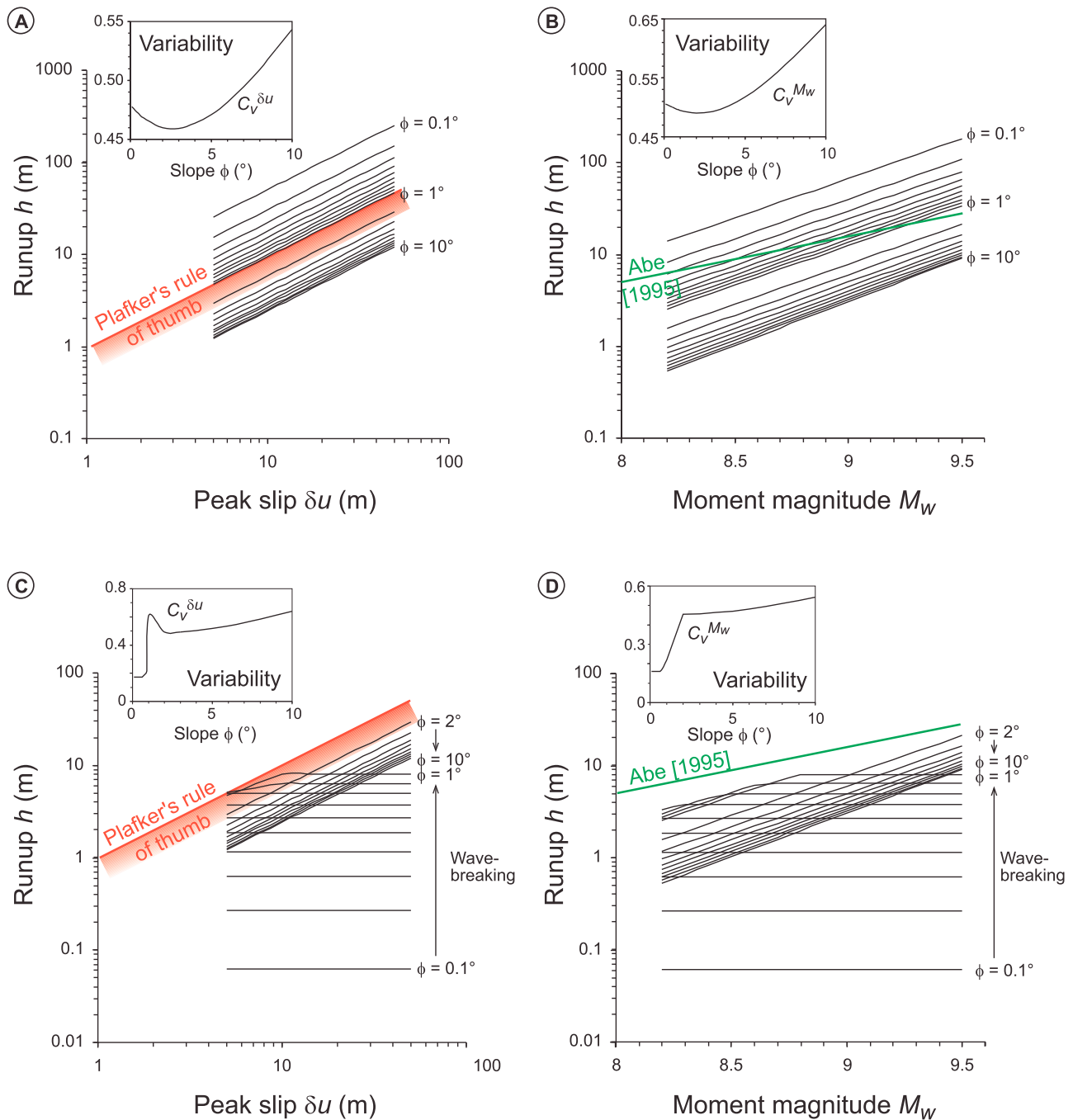
Figure 8. Intrinsic (Figures 8a and 8b) and effective (Figures 8c and 8d) scaling relationships for simulated tsunamis: (a) tsunami runup h as functions of peak earthquake slip δu and fore-arc slope ϕ in the nonbreaking wave regime, (b) tsunami runup h as functions of earthquake moment magnitude M_w and fore-arc slope ϕ in the nonbreaking wave regime, (c) tsunami runup h as functions of peak earthquake slip δu and fore-arc slope ϕ in the breaking wave regime, and (d) tsunami runup h as functions of earthquake moment magnitude M_w and fore-arc slope ϕ in the breaking wave regime (all parameter values are given at natural scale). Note that including wave breaking significantly limits the maximum wave heights such that empirical earthquake-tsunami scaling relationships are reproduced.

of thumb for ϕ ~1° dipping slope settings. However, equation (11) underestimates runup predicted by Plafker's rule of thumb for slopes $\phi > 1°$ and overestimates runup for slopes $\phi < 1°$ (Figure 8a). This inconsistency is partly

resolved by including wave breaking. Applying the limit criterion (equation (10)) produces a cutoff of the scaling relationship (Figure 8c) which yields a scaling relationship more consistent with the Plafker's rule of thumb. Note that
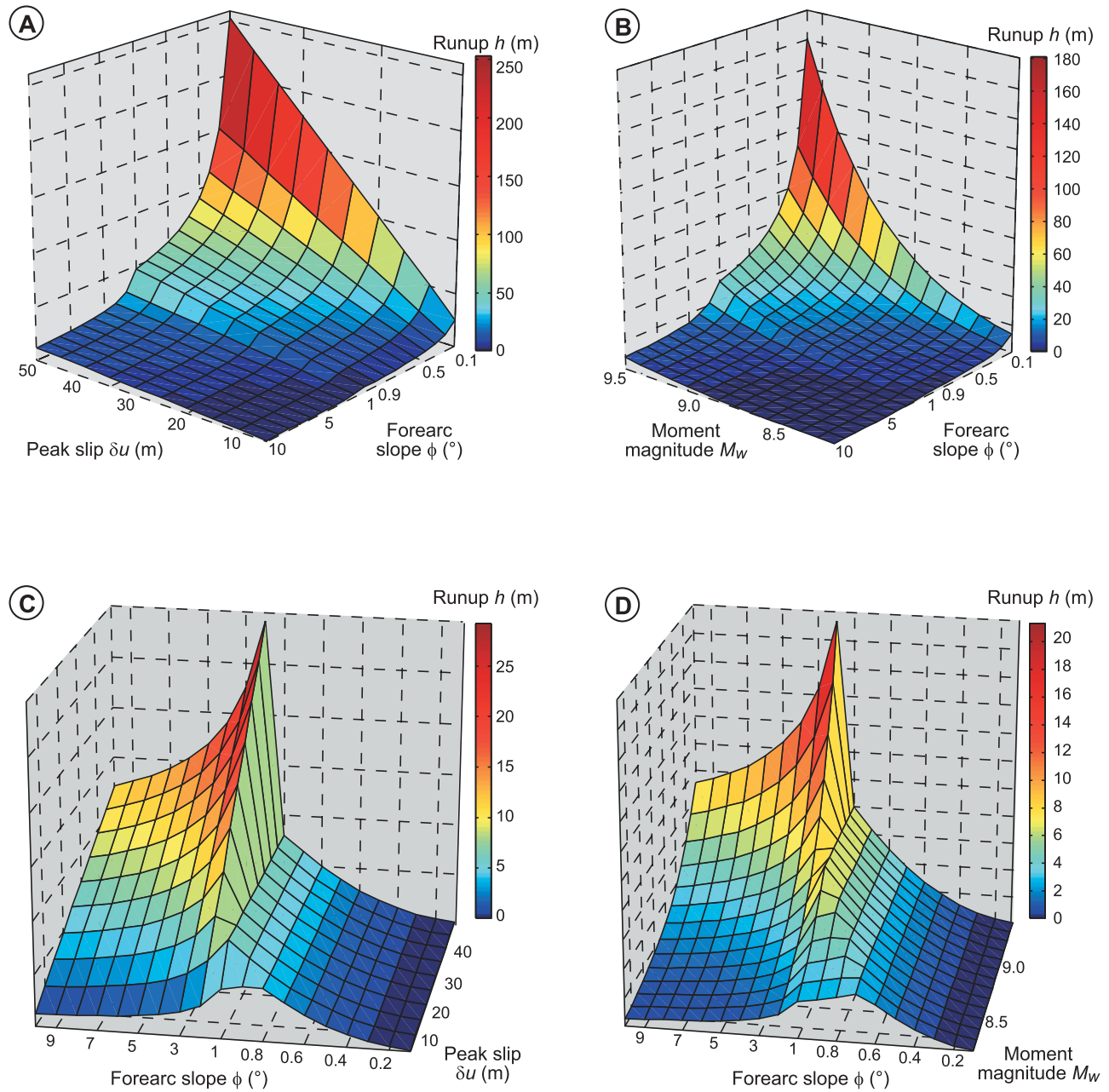
Figure 9. Three-dimensional visualizations of the intrinsic (Figures 9a and 9b) and effective (Figures 9c and 9d) scaling relationships for simulated tsunamis: (a) tsunami runup h as functions of peak earthquake slip δu and fore-arc slope ϕ if wave breaking is excluded, (b) tsunami runup h as functions of earthquake moment magnitude M_w and fore-arc slope ϕ if wave breaking is excluded, (c) tsunami runup h as functions of peak earthquake slip δu and fore-arc slope ϕ including wave breaking, and (d) tsunami runup h as functions of earthquake moment magnitude M_w and fore-arc slope ϕ including wave breaking (all parameter values are given at natural scale). Animated visualizations of Figures 9c and 9d can be found as dynamic content in the auxiliary material (Animations S1 and S2, respectively).

kick-in of the wave breaking limit depends both on the fore-arc slope and the peak slip resulting in a highly nonlinear scaling relationship (Figure 9c and Animation S1).

[34] While being consistent with earthquake slip-magnitude scaling, the intrinsic exponential $h(M_w)$ scaling (equation (12)) is inconsistent with natural observations.

The latter are represented here by an empirical scaling relationship for tsunami runup in the near field of the source inferred for $M_w \leq 9$ earthquakes in the Pacific, mostly Japan, by *Abe* [1981, 1995]:
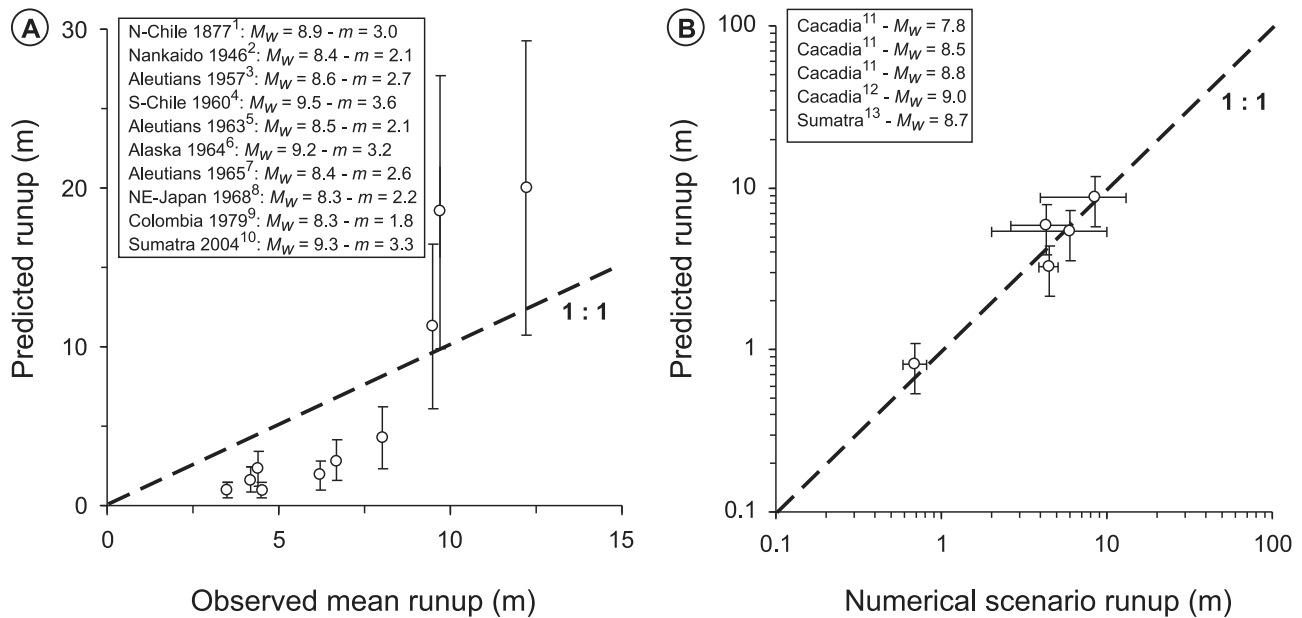
$$\log h = 0.5 M_w - 3.3 \qquad (14)$$

Figure 10. Validation and comparison of model predictions with (a) empirical data and (b) numerical scenario predictions. Dashed lines indicate 1:1 (perfect fit) reference; error bars indicate the standard deviation of the tsunami wavefield. See text for discussion. References: 1, *Kausel* [1986], *Gutierrez* [2003]; 2, *Satake* [1993] and *Abe* [1995]; 3, *Johnson and Satake* [1993] and *Lander* [1996]; 4, *Engdahl and Villasenor* [2002] and *Lockridge* [1985]; 5, *Beck and Ruff* [1987] and *Iida et al.* [1967]; 6, *Johnson et al.* [1996] and *Lander* [1996]; 7, *Johnson and Satake* [1996] and *Lander* [1996]; 8, *Kanamori* [1971] and *Abe* [1995]; 9, *Kanamori and Given* [1981] and *Geist* [2002]; 10, *Stein and Okal* [2007] and *Choi et al.* [2006]; 11, *Whitmore* [1993]; 12, *Geist and Parsons* [2006]; 13, *McCloskey et al.* [2008]. Here m denotes the Imamura-Iida tsunami magnitude which is the logarithm (base 2) of maximum tsunami height [*Iida et al.*, 1967].

Including wave breaking as a limiting process solves the inconsistencies resulting in a height cutoff (Figure 8d) very similar to equation (14). Since wave breaking kicks in most effectively at shallow sloping fore arcs ($\phi < 1$–$2°$) and for large magnitude earthquakes ($M_w > 8.5$) this results in a highly nonlinear scaling relationship (Figure 9d and Animation S2).

[35] Analysis of intrinsic and effective tsunami scaling behavior is an independent test of empirical scaling laws and demonstrates that the latter form a robust base for tsunami forecast models. Our simulation suggests that they yield a liberal estimate (i.e., an upper bound) of local tsunami runup even for giant ($M_w > 9$) events. They seem to be best applicable in moderately gentle sloping fore arcs ($\phi \sim 1$–$2°$). In shallower sloping settings, the empirical scaling relationships might actually overestimate tsunami runup significantly because waves tend to be reduced to lower heights than predicted by empirical scaling relationships due to wave breaking. However, as noted by *Synolakis* [1991], linear wave theory as applied here, might predict wave breaking for waves that do not actually break in nature. This might also explain the minor gaps between our effective scaling relationships and the empirical scaling relationships seen in Figures 8c and 8d. In more steeply dipping fore arcs, empirical scaling laws might overestimate tsunami runup because waves amplify less than predicted. Our analysis also highlights the importance of adequate treatment of wave breaking in simulating giant earthquake triggered local tsunamis. It is suggested that wave breaking is an utmost critical process in forecast models, particularly, in shallow sloping settings ($\phi < 1$–$2°$) and for earthquakes larger than $M_w \sim 8.5$.

4. Discussion

4.1. Model Validation: Comparison With Historical Events

[36] In order to validate our effective scaling relationships, we test their predictions using natural data from historical events. Particularly, we compare the tsunami runup predicted from the $h(M_w)$ scaling relationship including the effect of wave breaking (Figures 8d and 9d) using 10 earthquake-tsunami events in the moment magnitude range of our simulation (i.e., $M_w > 8.2$) that have a satisfactory observational record. Satisfaction in this context requires that the earthquake magnitude is well constrained and that the tsunami reports differentiate between the mean and maximum runup. Here we use the earthquake and tsunami data compiled by *Lay et al.* [1982] and *Geist* [2002] and data from the 1877 north Chile earthquake [*Kausel*, 1986; *Gutierrez*, 2003] and the 2004 Sumatra earthquake [*Stein and Okal*, 2007; *Choi et al.*, 2006]. Fore-arc slopes have been used from the survey of *Clift and Vannucchi* [2004], who report mean fore-arc slopes for distinct active margin segments averaged along profiles from the trench to >50 km continentward.

[37] A direct comparison of our runup predictions with natural runup data (Figure 10a) indicates that our model fits

observations reasonably well. A linear regression of predictions versus observations indicates a 13% overestimate of the actual runup if all events are included in the regression. However, the comparison reveals a systematic, bipolar bias: While runup of tsunamis with magnitude $m > 3$ (runup $h > 8$ m) has a tendency to be overestimated by our model, runup values $h < 8$ m (tsunami magnitude $m \leq 3$) are significantly larger than the predicted runup, i.e., not covered by the predicted standard deviation. We argue that this systematic bias is either an effect of incomplete hydrodynamic process similarity of our model or due to observational biases.

[38] With respect to the hydrodynamic process, our simulation neglects both the propagation stage of tsunami evolution and a possible leading depression wave. Because large-amplitude waves may attenuate more than small-amplitude waves during propagation [*Choi et al.*, 2006], neglecting this effect may yield the observed bias, i.e., larger runup for large tsunamis and smaller runup for small tsunamis. Preliminary results of an alternative, numerical tsunami model simulating the full hydrodynamic process more properly (see the auxiliary material) suggest that this effect is present but too small to explain the observed bias (Figure 7). Part of the overestimate of small runup could also be a result of the inappropriate application of a solitary wave model for the small natural events included in our data set. Assuming that the small tsunamis ($m \leq 3$) used in our comparison were triggered by earthquake slip further offshore than in our model, i.e., causing offshore subsidence and triggering a leading depression wave, this could account for ~1/3 higher runup than predicted by the solitary wave model [*Tadepalli and Synolakis*, 1996]. Taken together, model bias could account for at most 1/4 of the observed bias.

[39] Alternative (or additional) to model bias, observational bias could be present. Especially for less well surveyed and small events, tsunami intensity assessments may be biased toward extreme runup values. Where runup is in the scale of ocean waves and tidal variations, post tsunami surveys may focus on the more significant, measurable runup. The mean calculated from such subjectively influenced data would then not be representative and systematically overestimate actual runup. Moreover, runup may follow a lognormal distribution rather than a normal distribution [*Choi et al.*, 2006]. Consequently, the most observed value (the mode of the distribution) is always smaller than the mean of the sampled distribution. However, assuming a lognormal distribution with parameters as of *Choi et al.* [2006], bias due to incomplete sampling can be calculated to an underestimate of mean runup which is at most in the order of 10–20%.

[40] Finally, uncertainties in the estimates of earthquake amplitude and/or fore-arc slope could be present. Uncertainties in both parameters are amplified by the nonlinear earthquake-tsunami scaling relationships proposed here. This is particularly the case for slopes near 1°. Earthquake magnitude tends to be underestimated because of incomplete seismological data and different magnitude scales, particularly for preinstrumental events. Using the data on fore-arc slope given by *Clift and Vannucchi* [2004] slope might be overestimated as their measurement includes the generally steeper, near-trench slope of the fore-arc wedge. However, such uncertainties have minor impact for the events in

Figure 10a. In the earthquake magnitude and slope range considered here an underestimation of moment magnitude by 0.1 yields a ~20% underestimate of runup and a 1° overestimate of fore-arc slope results in ~15% underestimate in runup. Consequently, to account for the observed bias, moment magnitude would have to be underestimated by half a magnitude or, alternatively, slope would have to be overestimated by 7°. Both seem quantitatively unlikely to have occurred. However, uncertainties in estimates of slope and earthquake magnitude may add to model and observation biases to explain the systematic bias observed as a combined effect resulting from different sources.

[41] The recent great subduction megathrust earthquake that struck south central Chile on 27 February 2010 (Maule earthquake) may provide crucial constraints on the accuracy of our analog earthquake and tsunami models and the applicability of the proposed scaling relationship in the $M_w < 9$ range. The 2010 Maule earthquake nucleated near 36°S below the coast at ~35 km depth (U.S. Geological Survey, National Earthquake Information Center) and had a moment magnitude of $M_w = 8.8$ with a moment centered ~30 km offshore at 24 km depth on a 18° dipping thrust fault plane (Global CMT Project). Accordingly it meets the criteria for tsunamigenic earthquakes studied here (see section 3.1.2). The failed segment represents the northernmost part (33–38°S) of the accretionary margin of south Chile characterized by a fore-arc slope of 2.2° according to *Clift and Vannucchi* [2004]. Applying the proposed $h(M_w)$ scaling relationship we expect a local tsunami runup of $h = 4.7$ m ± 2.1m in average along the Chilean coast in the near field of the epicenter (~33–38°S). A comparison between this prediction and future results from posttsunami surveys will soon allow evaluating whether the underestimate of tsunami runup observed for smaller events ($M_w < 9$, $m < 3$) apparent from historic data analysis is related to model deficits or rather to insufficient data accuracy in the historical reports.

4.2. Cross Validation: Cascadia and Sumatra Case Scenarios

[42] Another way of assessing the accuracy of our forecast model is cross validation with existing numerical scenario simulations. We do this here for two well-studied settings: Sumatra [*McCloskey et al.*, 2008] and Cascadia [*Whitmore*, 1993; *Geist and Parsons*, 2006]. A direct comparison of runup predicted by our effective scaling relationship and spatially averaged values of numerical model predictions [*Whitmore*, 1993; *McCloskey et al.*, 2008; *Geist and Parsons*, 2006] indicates that the application of our $h(M_w)$ scaling relationship in combination with the fore-arc slope data from *Clift and Vannucchi* [2004] yields very consistent results (Figure 10b). In particular, the numerical predictions are reproduced within the 1-sigma standard deviation of our predictions. Noticeably, this consistency holds even when the scaling relationship is extrapolated down to $M_w < 8$ events, i.e., below the earthquake magnitude range of our simulation. The variability predicted by our scaling relationship is somewhat higher than predicted by numerical simulations presumably because of the inclusion of heterogeneity of coseismic fore-arc deformation in our simulation. For Cascadia, *Geist and Parsons* [2006] suggest a C_v ~ 0.14–0.25 while our model results in C_v ~0.25–0.3. Although our simplistic forecast model seem to match the
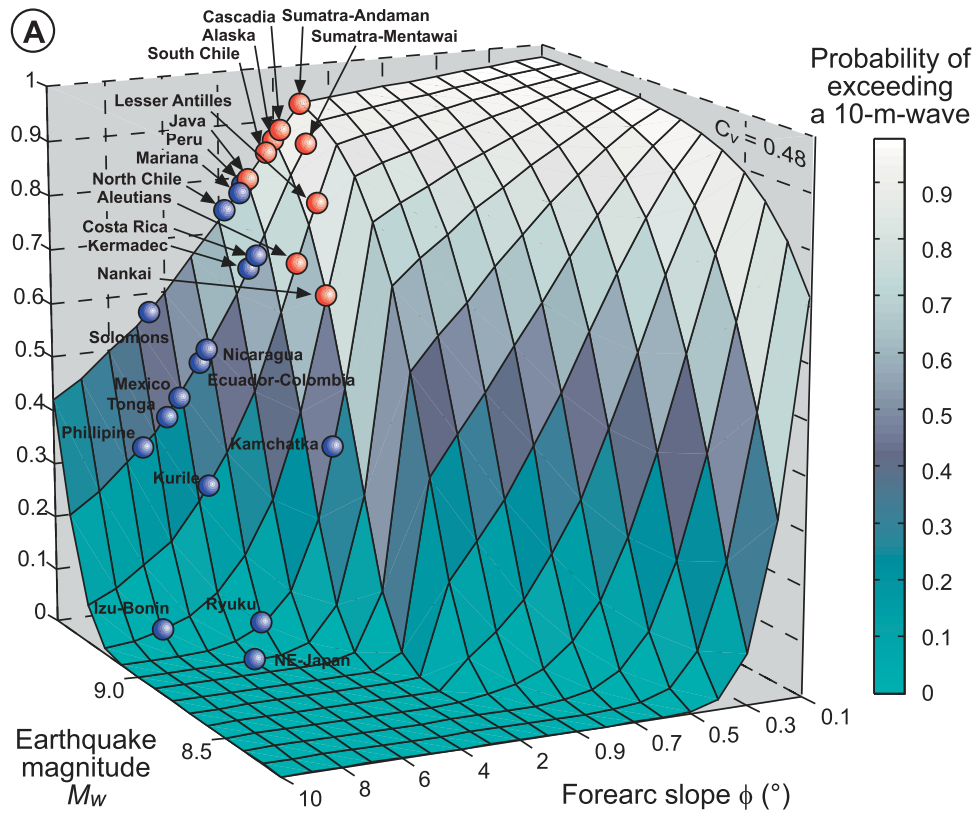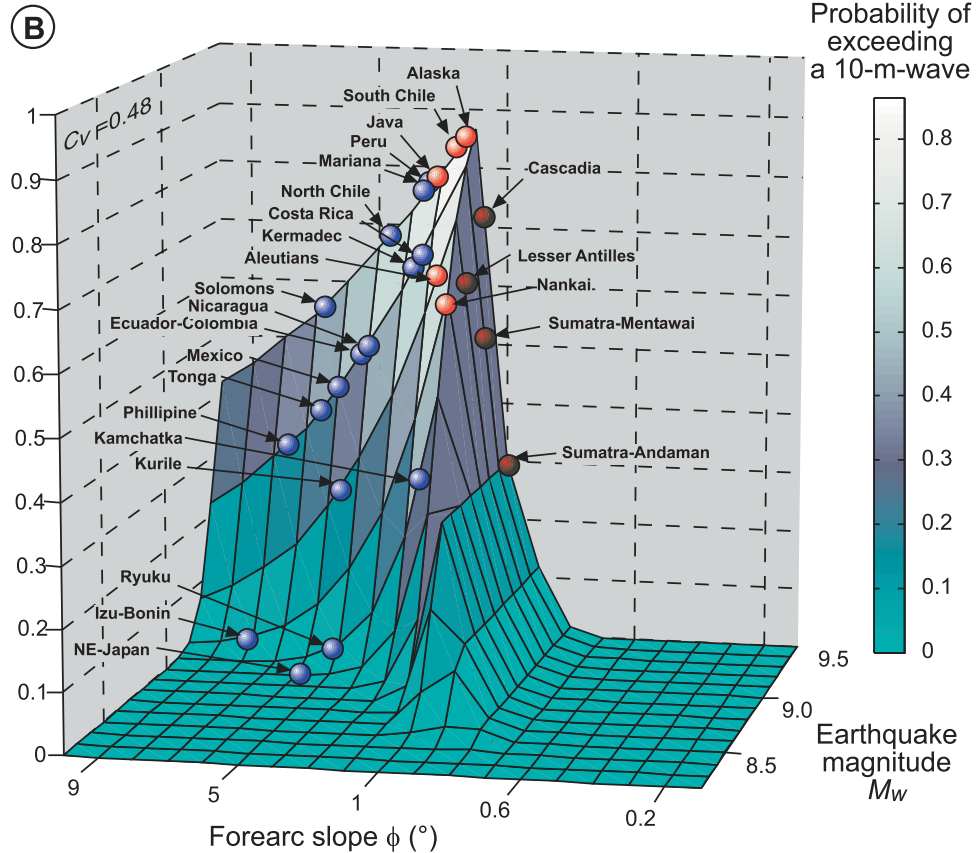
Figure 11

averaged predictions of elaborate tsunami simulations pretty well it is important to note that the strength of the latter is in predicting also the spatiotemporal details of runup along the coast.

4.3. Model Application: Global-Scale Analysis of Tsunami Susceptibility

[43] Using the size and variability of tsunamis predicted by our scaling relationships in combination with data on earthquake size and fore-arc anatomy allows the constraint of the first-order pattern of tsunami susceptibility related to giant megathrust earthquakes at a global scale. We base our susceptibility analysis both on the maximum earthquake magnitude that a specific subduction zone is capable to produce as inferred from plate kinematic and thermal constraints [*McCaffrey*, 2008], and on fore-arc slope data derived by analysis of geophysical data [*Clift and Vannucchi*, 2004]. We have calculated the probability of exceeding certain levels of tsunami runup along trench segments both in the nonbreaking wave and breaking wave regime. For the calculation we assumed that runup for a given earthquake magnitude is normally distributed around the mean with $C_v =$ 0.48. We emphasize that the probabilities derived here are conditioned to the occurrence of the greatest possible earthquake as given by *McCaffrey* [2008]. There is no information about the recurrence probability of such events (and therefore hazard) considered in our calculation.

[44] Accordingly, susceptibility shows a highly nonlinear behavior with dependencies on fore-arc slope, earthquake magnitude and the runup level of exceedence (Figure 11 and Animations S3 and S4). Figure 11 shows the probability of exceeding a tsunami with runup $h > 10$ m as a function of slope and earthquake magnitude with plate margins plotted at their respective positions. Noticeably, about half of the world's active margins have a probability for a tsunami runup in excess of 10 m which is higher than 50% in the event of the greatest possible earthquake.

[45] It becomes obvious that whereas all subduction zones are capable of producing giant earthquakes [*McCaffrey*, 2008], not all subduction zones are comparably susceptible to giant tsunamis as a consequence of wave amplification and breaking being sensitive to fore-arc slope. The latter varies significantly among different subduction zones (0.5 to 7.5° according to the analysis of *Clift and Vannucchi* [2004]) and is systematically related to subduction setting-specific parameters such as sediment fill in the trench and convergence velocity [*Clift and Vannucchi*, 2004]. In their assessment of mass transfer processes at active plate margins *Clift and Vannucchi* [2004] divided the present world subduction zones into those characterized by long-term (million year time scale) net crustal growth (accretionary

settings) and those where net loss of material occurred in the recent past (erosive settings). The first type of margins where sediment trench fill is accreted to the leading edge of the fore-arc wedge (e.g., south Chile, Alaska, Cascadia, Sunda) have generally relatively shallow sloping fore arcs (<3°). The second type of margins where material is eroded from the base of the fore-arc wedge (e.g., northern South America, Central America, Kuriles) tend to be steeper. This first-order pattern of subduction mode is directly reflected in the pattern of tsunami susceptibility. According to our analysis, accretionary margins (plotted red in Figure 11) are more susceptible to tsunamis than erosive margins (plotted blue in Figure 11). If wave breaking is excluded, tsunami disaster hot spots are south Chile, Sumatra-Mentawai, Sumatra-Andaman, Alaska and Cascadia. All of them are characterized by a ~90% chance that the occurrence of the largest possible earthquake triggers a tsunami with runup >10 m. Including the effect of wave breaking shows that tsunami hazard in three of them (Sumatra-Andaman, Sumatra-Mentawai and Cascadia) may be significantly reduced as the maximum wave height might be limited in these very shallow sloping margin settings. However, because of the strong sensitivity of the scaling relationships to fore-arc slopes in the range $1° < \phi < 2°$, inferences have to be drawn here with caution.

[46] The probabilities derived here are conditioned to the occurrence of a giant earthquake. Therefore tsunami hazard in terms of a time-dependent forecast is controlled by the recurrence pattern and period of such events. Three out of the top five giant earthquake-triggered tsunami disaster hot spots spotted by our analysis had great to giant earthquakes in the last decades (1960 and 2010 Chile, 1964 Alaska, 2004 Burma-Andaman) and are unlikely to rerupture in the next few decades if a quasiperiodic recurrence pattern is assumed [e.g., *Sykes and Menke*, 2006]. South of the 2004 Sumatra-Andaman earthquake, the Sunda megathrust just started releasing strain by partial failure generating earthquakes of magnitude $M_w \sim 8$ and only small tsunamis (2005 and 2007, no fatalities [*McAdoo et al.*, 2006; *Borrero et al.*, 2007]). These earthquakes were probably the beginning of a sequence of large (but not giant) events breaking the Sunda plate interface in the next decades [*Sieh et al.*, 2008]. Cascadia remains a major future tsunami disaster hot spot.

[47] We recall that the global assessment presented here considers susceptibility to giant megathrust earthquake-triggered tsunamis only. Since this type of events is relatively infrequent (1–3 per century according to *McCaffrey* [2008]) it represents only a fraction of the effective hazard related to tsunamis from all possible sources. Particularly, tsunamis triggered by volcanic eruptions, submarine landslides and other type of earthquakes might be similar in size

---

Figure 11. Global distribution of susceptibility to giant subduction megathrust earthquake-triggered tsunami if wave breaking is (a) excluded and (b) included. Surfaces represent the probability of exceeding a 10 m tsunami runup as a function of fore-arc slope and earthquake magnitude. Distinct active margins are indicated by balls (red indicates accretionary settings; blue indicates erosive settings) with their specific location constraint by the fore-arc slope as given by *Clift and Vannucchi* [2004] and the maximum earthquake size as determined by *McCaffrey* [2008]. Accordingly, tsunami disaster hot spots occur predominantly along accretionary margins (Sumatra, Cascadia, Alaska, and south Chile). Note that tsunami hazard is significantly reduced for the shallow dipping ($\phi < 1-2°$) fore arcs if wave breaking is included. Animated visualization of the probability surfaces in Figures 11a and 11b for different levels of exceedence can be found in Animations S3 and S4 in the auxiliary material, respectively.

as the tsunamis simulated here (runup about 10 m) but more frequent phenomena. For example, the Aleutians, northeast Japan and the Kuriles have relatively high tsunami hazard because of the historical occurrence of anomalous large tsunamis (compared to their parent earthquake magnitude) triggered by so-called "tsunami earthquakes," which are relatively slow (<2 km/s rupture velocity) and shallow (<20 km depth) megathrust slip events [*Kanamori*, 1972, *Geist and Bilek*, 2001; *Bilek and Lay*, 2002]. Similar seismic events with smaller or not reported tsunamis are also known from Peru, Nicaragua, Tonga, Java, Kamchatka and Mexico [*Geist*, 2002; *Okal*, 2009]. Importantly also, the Aegean, New Hebrides, Hikurangi (New Zealand) and Luzon arc (including Taiwan) margins are not considered in the present analysis because of missing data on fore-arc slope. All of them are capable of producing giant $M_w > 9$ earthquakes [*McCaffrey*, 2008]. The historic earthquake and tsunami record [*Lay et al.*, 1982; *Geist*, 2002; *Stein and Okal*, 2007] is, however, characterized by only moderate earthquakes M7–M8 earthquakes and tsunamis in these regions (e.g., New Hebrides, 1965, *M*7.6, tsunami runup ~3.5 m [*Ebel*, 1980; *Lockridge and Smith*, 1984]).

5. Conclusions

[48] We have studied the scaling behavior of local tsunamis triggered by giant subduction megathrust earthquakes using an analog model of a subduction fore arc in combination with linear wave theory. Based on the coseismic surface deformation during a sequence of experimentally simulated megathrust earthquakes and a simple tsunami model following *Tanioka and Satake* [1996] and *Synolakis* [1987, 1991], we have derived scaling relationships for local tsunami runup as a function of earthquake peak slip, moment magnitude and fore-arc wedge slope. Intrinsically, local tsunami runup scales linearly with peak earthquake slip, exponentially with moment magnitude, and according to an inverse power law to fore-arc slope. The variability of local tsunami runup is controlled by heterogeneity in earthquake slip, slip partitioning, and strain localization. It is characterized by a coefficient of variation $C_v \sim 0.5$ which is reduced to $C_v \sim 0.2$ at gently sloping margins (<1–2°), where wave breaking limits possible tsunami heights. To honor wave breaking as a critical process in tsunami scaling, we present an effective scaling relationship including a wave breaking criterion of *Synolakis* [1991]. It reproduces natural observations, existing scenario predictions as well as empirical scaling relationships. Our analysis supports forecast models based on empirical scaling relationships and demonstrates that the latter are liberal estimates of tsunami hazard. They appear to be robust estimates of tsunami runup up to M_w 9.5 and are best applicable in accretionary subduction settings where the fore-arc slope is moderately gentle (<1–2°). Tsunami susceptibility analysis using global data sets of fore-arc slope [*Clift and Vannucchi*, 2004] and setting-specific maximum earthquake size [*McCaffrey*, 2008] suggest that about half of the world's subduction zones have a >50% probability of a tsunami runup >10 m in the event of the greatest possible earthquake in the region. Tsunami disaster hot spots occur preferentially along accretionary plate margins (Sunda, Alaska, south Chile, Cascadia).

Notation

a' coseismic acceleration, m/s^2.
a-b friction rate parameter.
α fitting parameter.
β fitting parameter.
C cohesion, Pa.
Ca Cauchy number.
C_v coefficient of variation.
d water depth, m.
η viscosity, Pa s.
Fr Froude number.
g gravitational acceleration, m/s^2.
G gravitation, N.
h tsunami runup, m.
h_{max} limited wave height, m.
H initial wave height, m.
I inertia, N.
k bulk modulus, Pa.
L characteristic length, m.
L dimension of length.
μ friction coefficient.
m tsunami magnitude.
M dimension of mass.
M_0 seismic moment, N m.
M_w moment magnitude.
ϕ fore-arc slope, deg.
R^2 coefficient of determination.
ρ density, kg/m^3.
σ strength, Pa.
t characteristic time, s.
τ strength ratio.
T dimension of time.
Γ strength contrast.
δu peak earthquake slip, m.
du displacement, m.
v interseismic velocity, m/s.
v' coseismic velocity, m/s.
V rock volume, m^3.
W characteristic width, m.
x trench distance, m.

References

Abe, K. (1981), Physical size of tsunamigenic earthquakes of the northwestern Pacific, *Phys. Earth Planet. Inter.*, 27, 194–205, doi:10.1016/0031-9201(81)90016-9.

Abe, K. (1995), Estimate of tsunami run-up heights from earthquake magnitudes, in *Tsunami: Progress in Prediction, Disaster Prevention and Warning*, *Adv. Nat. Technol. Hazards Res*, vol. 4, edited by Y. Tsuchiya and N. Shuto, pp. 21–35, Kluwer Acad., Norwell, Mass.

Adam, J., J. L. Urai, B. Wieneke, O. Oncken, K. Pfeiffer, N. Kukowski, J. Lohrmann, S. Hoth, W. van der Zee, and J. Schmatz (2005), Shear localization and strain distribution during tectonic faulting—New insights from granular-flow experiments and high-resolution optical image correlation techniques, *J. Struct. Geol.*, 27, 283–301, doi:10.1016/j.jsg.2004.08.008.

Beck, S. L., and L. J. Ruff (1987), Rupture process of the 1963 Kurile Islands earthquake sequence: Asperity interaction and multiple event

rupture, *J. Geophys. Res.*, *92*, 14,123–14,138, doi:10.1029/JB092iB13p14123.

Bilek, S. L., and T. Lay (2002), Tsunami earthquakes possibly widespread manifestations of frictional conditional stability, *Geophys. Res. Lett.*, *29*(14), 1673, doi:10.1029/2002GL015215.

Borrero, J. C., R. Hidayat, Suranto, C. Bosserelle, and E. A. Okal (2007), Field survey and preliminary modeling of the near-field tsunami from the Bengkulu earthquake of 12 September 2007, *Eos Trans. AGU*, *88*(52), Fall Meet. Suppl., Abstract U54A-04.

Byrne, D. E., D. M. Davis, and L. R. Sykes (1988), Loci and maximum size of thrust earthquakes and the mechanics of the shallow region of subduction zones, *Tectonics*, *7*, 833–857, doi:10.1029/TC007i004p00833.

Chauhan, A. P. S., et al. (2009), Seismic imaging of forearc backthrusts at northern Sumatra subduction zone, *Geophys. J. Int.*, *179*, 1772–1780, doi:10.1111/j.1365-246X.2009.04378.x.

Choi, B. H., S. J. Hong, and E. Pelinovsky (2006), Distribution of runup heights of the December 26, 2004 tsunami in the Indian Ocean, *Geophys. Res. Lett.*, *33*, L13601, doi:10.1029/2006GL025867.

Clift, P., and V. Vannucchi (2004), Controls on tectonic accretion versus erosion in subduction zones: Implications for the origin and recycling of the continental crust, *Rev. Geophys.*, *42*, RG2001, doi:10.1029/2003RG000127.

Cloos, M. (1992), Thrust-type subduction-zone earthquakes and seamount asperities: A physical model for seismic rupture, *Geology*, *20*, 601–604, doi:10.1130/0091-7613(1992)020<0601:TTSZEA>2.3.CO;2.

Ebel, J. E. (1980), Source processes of the 1965 New Hebrides Islands earthquakes inferred from teleseismic waveforms, *Geophys. J. R. Astron. Soc.*, *63*, 381–403.

Engdahl, E., and A. Villaseñor (2002), Global seismicity: 1900–1999, in *International Handbook of Earthquake and Engineering Seismology*, *Int. Geophys. Ser*, vol. 81, edited by W. H. K. Lee et al., pp. 665–690, doi:10.1016/S0074-6142(02)80244-3, Academic, Amsterdam.

Freund, L. B., and D. M. Barnett (1976), A two-dimensional analysis of surface deformation due to dip-slip faulting, *Bull. Seismol. Soc. Am.*, *66*(3), 667–675.

Geist, E. L. (2002), Complex earthquake rupture and local tsunamis, *J. Geophys. Res.*, *107*(B5), 2086, doi:10.1029/2000JB000139.

Geist, E. L., and S. L. Bilek (2001), Effect of depth-dependent shear modulus on tsunami generation along subduction zones, *Geophys. Res. Lett.*, *28*(7), 1315–1318, doi:10.1029/2000GL012385.

Geist, E. L., and R. Dmowska (1999), Local tsunamis and distributed slip at the source, *Pure Appl. Geophys.*, *154*, 485–512, doi:10.1007/s000240050241.

Geist, E. L., and T. Parsons (2006), Probabilistic analysis of tsunami hazards, *Nat. Hazards*, *37*, 277–314, doi:10.1007/s11069-005-4646-z.

Geist, E. L., et al. (2007), Implications of the 26 December 2004 Sumatra–Andaman earthquake on tsunami forecast and assessment models for great subduction-zone earthquakes, *Bull. Seismol. Soc. Am.*, *97*(1A), S249–S270, doi:10.1785/0120050619.

González, F. I., K. Satake, E. F. Boss, and H. O. Mofjeld (1995), Edge wave and non-trapped modes of the 25 April 1992 Cape Mendocino Tsunami, *Pure Appl. Geophys.*, *144*(3–4), 409–426, doi:10.1007/BF00874375.

Gutierrez, D. (2003), Advances in the Chilean tsunami warning system and application of the TIME project to the Chilean coast, in *Early Warning Systems for Natural Disaster Reduction*, edited by J. Zschau and A. N. Küppers, pp. 543–548, Springer, New York.

Hoechner, A., A. Y. Babeyko, and S. V. Sobolev (2008), Enhanced GPS inversion technique applied to the 2004 Sumatra earthquake and tsunami, *Geophys. Res. Lett.*, *35*, L08310, doi:10.1029/2007GL033133.

Hubbert, M. K. (1937), Theory of scale models as applied to the study of geological structures, *Geol. Soc. Am. Bull.*, *48*, 1459–1520.

Iida, K., D. C. Cox, and G. Pararas-Carayannis (1967), Preliminary catalog of tsunamis occurring in the Pacific Ocean, *Data Rep. 5, HIG-67-10*, 274 pp., Univ. of Hawaii, Honolulu.

Johnson, J. M., and K. Satake (1993), Source parameters of the 1957 Aleutian earthquake from tsunami waveforms, *Geophys. Res. Lett.*, *20*, 1487–1490, doi:10.1029/93GL01217.

Johnson, J. M., and K. Satake (1996), The 1965 Rat Islands earthquake: A critical comparison of seismic and tsunami wave inversions, *Bull. Seismol. Soc. Am.*, *86*, 1229–1237.

Johnson, J. M., K. Satake, S. R. Holdahl, and J. Sauber (1996), The 1964 Prince William Sound earthquake: Joint inversion of tsunami and geodetic data, *J. Geophys. Res.*, *101*, 523–532, doi:10.1029/95JB02806.

Kanamori, H. (1971), Focal mechanism of the Tokachi-Oki earthquake of May 16, 1968: Contortion of the lithosphere at a junction of two trenches, *Tectonophysics*, *12*, 1–13, doi:10.1016/0040-1951(71)90063-1.

Kanamori, H. (1972), Mechanism of tsunami earthquakes, *Phys. Earth Planet. Inter.*, *6*, 346–359, doi:10.1016/0031-9201(72)90058-1.

Kanamori, H., and J. W. Given (1981), Use of long-period surface waves for fast determination of earthquake source parameters, *Phys. Earth Planet. Inter.*, *27*, 8–31, doi:10.1016/0031-9201(81)90083-2.

Kausel, E. (1986), Los terremotos de agosto de 1869 y mayo de 1977 que afectaron el Sur de Peru y Norte de Chile, *Bol. 3*(2), pp. 8–13, Acad. Chilena Cienc., Univ. Santiago, Santiago, Chile.

Klingelhoefer, F., et al. (2010), Limits of the seismogenic zone in the epicentral region of the 26 December 2004 great Sumatra-Andaman earthquake: Results from seismic refraction and wide-angle reflection surveys and thermal modeling, *J. Geophys. Res.*, *115*, B01304, doi:10.1029/2009JB006569.

Kopp, H., and N. Kukowski (2003), Backstop geometry and accretionary mechanics of the Sunda margin, *Tectonics*, *22*(6), 1072, doi:10.1029/2002TC001420.

Lander, J. F. (1996), Tsunamis affecting Alaska 1737–1996, *NGDC Key Geophys. Res. Doc. 31*, 195 pp., Natl. Geophys. Data Cent., NOAA, Boulder, Colo.

Lay, T., H. Kanamori, and L. Ruff (1982), The asperity model and the nature of large subduction zone earthquakes, *J. Earthquake Predict. Res.*, *1*, 3–71.

Lockridge, P. A. (1985), Tsunamis in Peru-Chile, *Publ. SE-39*, 97 pp., World Data Cent. A for Solid Earth Geophys., Natl. Geophys. Data Cent., NOAA, Boulder, Colo.

Lockridge, P. A., and R. H. Smith (1984), Tsunamis in the Pacific Basin, 1900–1983, Natl. Geophys. Data Cent., NOAA, Boulder, Colo.

Lohrmann, J., et al. (2003), The impact of analog material properties on the geometry, kinematics, and dynamics of convergent sand wedges, *J. Struct. Geol.*, *25*, 1691–1711, doi:10.1016/S0191-8141(03)00005-1.

McAdoo, B. G., L. Dengler, G. Prasetya, and V. Titov (2006), Smong: How an oral history saved thousands on Indonesia's Simeulue Island during the December 2004 and March 2005 tsunamis, *Earthquake Spectra*, *22*, S661–S669, doi:10.1193/1.2204966.

McCaffrey, R. (2008), Global frequency of magnitude 9 earthquakes, *Geology*, *36*, 263–266, doi:10.1130/G24402A.1.

McCloskey, J., A. Antonioli, A. Piatanesi, K. Sieh, S. Steacy, S. S. Nalbant, M. Cocco, C. Giunchi, J. Huang, and P. Dunlop (2008), Tsunami threat in the Indian Ocean from a future megathrust earthquake west of Sumatra, *Earth Planet. Sci. Lett.*, *265*, 61–81, doi:10.1016/j.epsl.2007.09.034.

Meltzner, A. J., K. Sieh, M. Abrams, D. C. Agnew, K. W. Hudnut, J.-P. Avouac, and D. H. Natawidjaja (2006), Uplift and subsidence associated with the great Aceh-Andaman earthquake 2004, *J. Geophys. Res.*, *111*, B02407, doi:10.1029/2005JB003891.

Moreno, M. S., J. Bolte, J. Klotz, and D. Melnick (2009), Impact of megathrust geometry on inversion of coseismic slip from geodetic data: Application to the 1960 Chile earthquake, *Geophys. Res. Lett.*, *36*, L16310, doi:10.1029/2009GL039276.

Nicol, A., and J. Beavan (2003), Shortening of an overriding plate and its implications for slip on a subduction thrust, central Hikurangi Margin, New Zealand, *Tectonics*, *22*(6), 1070, doi:10.1029/2003TC001521.

Okada, Y. (1992), Internal deformation due to shear and tensile faults in a half-space, *Bull. Seismol. Soc. Am.*, *82*, 1018–1040.

Okal, E. A. (2009), Excitation of tsunamis by earthquakes, in *The Sea*, vol. 15, *Tsunamis*, 1st ed., edited by E. N. Bernard and A. R. Robinson, pp. 137–177, Wiley-Interscience, New York.

Okal, E. A., and C. E. Synolakis (2003), A theoretical comparison of tsunamis from dislocations and landslides, *Pure Appl. Geophys.*, *160*, 2177–2188, doi:10.1007/s00024-003-2425-x.

Okal, E. A., and C. E. Synolakis (2004), Source discriminants for near-field tsunamis, *Geophys. J. Int.*, *158*, 899–912, doi:10.1111/j.1365-246X.2004.02347.x.

Oleskevich, D. A., R. D. Hyndman, and K. Wang (1999), The updip and downdip limits to great subduction earthquakes: Thermal and structural models of Cascadia, south Alaska, SW Japan, and Chile, *J. Geophys. Res.*, *104*(B7), 14,965–14,991, doi:10.1029/1999JB900060.

Park, S.-C., T. Tsuru, S. Kodaira, P. R. Cummins, and Y. Kaneda (2002), Splay fault branching at the Nankai subduction zone, *Science*, *297*, 1157–1160, doi:10.1126/science.1074111.

Plafker, G. (1972), Alaskan earthquake of 1964 and Chilean earthquake of 1960: Implications for arc tectonics, *J. Geophys. Res.*, *77*, 901–925, doi:10.1029/JB077i005p00901.

Plafker, G. (1997), Catastrophic tsunami generated by submarine slides and backarc thrusting during the 1992 earthquake on Eastern Flores, Indonesia, *Geol. Soc. Am. Abstr. Programs*, *29*(5), 57.

Rosenau, M., and O. Oncken (2009), Fore-arc deformation controls frequency-size distribution of megathrust earthquakes in subduction zones, *J. Geophys. Res.*, *114*, B10311, doi:10.1029/2009JB006359.

Rosenau, M., J. Lohrmann, and O. Oncken (2009), Shocks in a box: An analogue model of subduction earthquake cycles with application to seis-

motectonic forearc evolution, *J. Geophys. Res.*, *114*, B01409, doi:10.1029/2008JB005665.

Ruff, L. J., and B. Tichelaar (1996), What controls the seismogenic plate interface in subduction zones?, in *Subduction: Top to Bottom*, *Geophys. Monogr. Ser.*, vol. 96, edited by G. E. Bebout et al., pp. 105–111, AGU, Washington, D. C.

Satake, K. (1993), Depth distribution of coseismic slip along the Nankai trough, Japan, from joint inversion of geodetic and tsunami data, *J. Geophys. Res.*, *98*, 4553–4565, doi:10.1029/92JB01553.

Scholz, C. H. (1998), Earthquakes and friction laws (1998), *Nature*, *391*, 37–42, doi:10.1038/34097.

Shreve, R. L., and M. Cloos (1986), Dynamics of sediment subduction, melange formation, and prism accretion, *J. Geophys. Res.*, *91*(B10), 10,229–10,245, doi:10.1029/JB091iB10p10229.

Sieh, K., et al. (2008), Earthquake supercycles inferred from sea-level changes recorded in the corals of West Sumatran, *Science*, *322*, 1674–1678, doi:10.1126/science.1163589.

Singh, S. C., et al. (2010), Evidence of active backthrusting at the NE margin of Mentawai Islands, SW Sumatra, *Geophys. J. Int.*, *180*, 703–714, doi:10.1111/j.1365-246X.2009.04458.x.

Sobolev, S. V., A. Y. Babeyko, R. Wang, A. Hoechner, R. Galas, M. Rothacher, D. V. Sein, J. Schröter, J. Lauterjung, and C. Subarya (2007), Tsunami early warning using GPS-Shield arrays, *J. Geophys. Res.*, *112*, B08415, doi:10.1029/2006JB004640.

Stein, S., and E. A. Okal (2007), Ultralong period seismic study of the December 2004 Indian Ocean earthquake and implications for regional tectonics and the subduction process, *Bull. Seismol. Soc. Am.*, *97*, S279–S295, doi:10.1785/0120050617.

Sykes, L. R., and W. Menke (2006), Repeat times of large earthquakes: Implications for earthquake mechanics and long-term prediction, *Bull. Seismol. Soc. Am.*, *96*, 1569–1596, doi:10.1785/0120050083.

Synolakis, C. E. (1987), The runup of solitary waves, *J. Fluid Mech.*, *185*, 523–545, doi:10.1017/S002211208700329X.

Synolakis, C. E. (1991), Tsunami runup on steep slopes: How good linear theory really is, *Nat. Hazards*, *4*, 221–234, doi:10.1007/BF00162789.

Tadepalli, S., and C. E. Synolakis (1994), The run-up of N-waves on sloping beaches, *Proc. R. Soc. London A*, *445*, 99–112, doi:10.1098/rspa.1994.0050.

Tadepalli, S., and C. E. Synolakis (1996), Model for the leading waves of tsunamis, *Phys. Rev. Lett.*, *77*(10), 2141–2144, doi:10.1103/PhysRevLett.77.2141.

Tanioka, Y., and K. Satake (1996), Tsunami generation by horizontal displacement of ocean bottom, *Geophys. Res. Lett.*, *23*(8), 861–864, doi:10.1029/96GL00736.

Völker, D., et al. (2007), Latitudinal variation in sedimentary processes in the Peru-Chile Trench off central Chile, in The Andes—Active Subduction Orogeny, *Front. Earth Sci. Ser.*, vol. 1, edited by O. Oncken et al., pp. 193–216, Springer, Berlin.

von Huene, R., and D. Klaeschen (1999), Opposing gradients of permanent strain in the aseismic zone and elastic strain across the seismogenic zone of the Kodiak shelf and slope, Alaska, *Tectonics*, *18*(2), 248–262, doi:10.1029/1998TC900022.

Wang, K., and J. He (2008), Effects of frictional behavior and geometry of subduction fault on coseismic seafloor deformation, *Bull. Seismol. Soc. Am.*, *98*(2), 571–579, doi:10.1785/0120070097.

Wang, K., and Y. Hu (2006), Accretionary prisms in subduction earthquake cycles: The theory of dynamic Coulomb wedge, *J. Geophys. Res.*, *111*, B06410, doi:10.1029/2005JB004094.

Whitmore, P. M. (1993), Expected tsunami amplitude and currents along the North American Coast for Cascadia subduction zone earthquakes, *Nat. Hazards*, *8*, 59–73, doi:10.1007/BF00596235.

Wells, R. E., R. J. Blakely, Y. Sugiyama, D. W. Scholl, and P. A. Dinterman (2003), Basin-centered asperities in great subduction zone earthquakes: A link between slip, subsidence, and subduction erosion?, *J. Geophys. Res.*, *108*(B10), 2507, doi:10.1029/2002JB002072.

Yeh, H. (1991), Tsunami bore run-up, *Nat. Hazards*, *4*, 209–220, doi:10.1007/BF00162788.

S. Brune, Department of Physics of the Earth, Helmholtz-Centre Potsdam, GFZ German Research Centre for Geosciences, Telegrafenberg, D-14473 Potsdam, Germany.

R. Nerlich, Simula Research Laboratory, PO Box 134, N-1325 Lysaker, Norway.

O. Oncken and M. Rosenau, Department of Geodynamics, Helmholtz-Centre Potsdam, GFZ German Research Centre for Geosciences, Telegrafenberg, D-14473 Potsdam, Germany. (rosen@gfz-potsdam.de)